TECHNISCHE UNIVERSITÄT MÜNCHEN

Master's Thesis in Physics

Final Acceptance Testing of the Precision Optical Calibration Module for the IceCube Upgrade

Patrick Schaile

2nd September 2024

Supervisor: Prof. Dr. Elisa Resconi

Advisors: Dr. Andrii Terliuk
Dr. Philipp Eller
Dr. Simeon Bash

Abstract

In the context of the IceCube Upgrade, which mainly aims to improve and extend the scientific capabilities of the IceCube Neutrino Observatory, the Precision Optical Calibration Module, POCAM, has been developed. It is an isotropic, self-monitoring calibration light source, which will be deployed into the Antarctic ice as a new part of the detector and is meant to investigate and determine the optical detector systematics to high precision. The improved knowledge on parameters like absorption or scattering length will eventually lead to likewise improved detector sensitivity and data analyses. This thesis focuses on the characterization procedure and final acceptance testing for the first six POCAM devices, covering the used setups, including all necessary equipment, software efforts to develop a procedure as automated as possible, the calibration and characterization process and results for the first batch, as well as technical difficulties and adjustments encountered throughout. The thesis further offers a comprehensive overview on the project's physics background, the IceCube Neutrino Observatory, and the POCAM device itself, including its motivation and design. Finally, it concludes with a summary of the results and provides an outlook on the project's future.

Contents

1. Introduction

Neutrino Astronomy is one of the most promising research fields in physics due to a variety of reasons. It combines the capability to investigate large and complex structures at vast distances, such as black holes, supernovae, or even entire galaxies, with fundamental research into the properties of the particles themselves. For the former, neutrino detectors may contribute as one branch of a Multi-Messenger Astronomy, that comprises the detection of photons, neutrinos and other particles, or even gravitational waves. Some of the most prominent results of incorporating the detection of astrophysical neutrinos to a Multi-Messenger Astronomy, include the identification of neutrino point sources. These sources encompass the blazars TXS $0506+056$ and PKS $1424+240$, the galaxy NGC 1068, as well as the Galactic plane, all of which have exhibited an excess in neutrino emission, making them plausible neutrino sources [1–3]. Apart from utilizing neutrinos as cosmic messengers to gain more information about their origins, one might also focus on the underlying physics of these particles. That is, large-area neutrino detectors, like the IceCube Neutrino Observatory, can also be used to study the more fundamental behavior of neutrinos, such as the phenomenon of neutrino oscillations and associated parameters, like neutrino masses and mixing angles, which remains an active field of research in particle physics. The determination of such parameters, as well as the progress in investigating high-energy astrophysical neutrinos, require adequate resolution and a thorough understanding of detector systematics. To account for this in IceCube, the Precision Optical Calibration Module (POCAM), has been developed. It is an isotropic, self-monitoring calibration light source, which will be deployed into the Antarctic ice as a new part of the detector and is meant to investigate and determine the optical detector systematics to high precision. 21 devices are planned to be installed in the polar season 2025/26 in the context of the IceCube Upgrade, which aims to improve and extend the detector's scientific capabilities. This thesis is about the work and process of the characterization procedure and final acceptance testing for the first six produced POCAM devices. Finally, the thesis contents are outlined as follows.

Chapter 2: Neutrino Physics
To establish the general context, this chapter begins with a brief overview of both known and potential neutrino sources that could ultimately generate signals in

neutrino detectors, like IceCube. Special focus lies on atmospheric and astrophysical neutrinos, as they are the most important ones for IceCube. It further contains a discussion on fundamental neutrino physics within and beyond the Standard Model, including basic interaction processes and the effect of neutrino oscillations.

Chapter 3: IceCube Neutrino Observatory
With IceCube being a central aspect for the work of this thesis, this part introduces the detector. This includes an overview on the detector design and the basic detection principles. As POCAM is developed as a calibration device that will be deployed in the context of the detector's Upgrade, this chapter discusses the main systematic detector effects and the IceCube Upgrade.

Chapter 4: Precision Optical Calibration Module (POCAM)
This part introduces the POCAM device, covering the motivation for its development as well as its physical concept and device design.

Chapter 5: POCAM Characterization Procedure
This chapter contains the main part and was the focus of the work for this thesis. It presents the complete structure of the characterization procedure for POCAM. Besides the general structure, including the measurement setups and its working principle, it covers the results for the characterization and final acceptance testing of the first six POCAM devices.

Chapter 6: Conclusion
The thesis closes with a summary of the most important results and concludes the characterizaion of the first batch of POCAMs. Finally it gives an outlook for future characterizations that will be conducted for the remaining devices and the outlines the future of POCAM as part of the IceCube Upgrade.

2. Neutrino Physics

2.1. Neutrino Origins

A well known source of neutrinos is radioactive decay, where the mechanism responsible for producing the particles is the beta decay

$$n \rightarrow p + e^- + \bar{\nu}_e \tag{2.1}$$

Historically, the recognition of the beta decay as a three-body process led Wolfgang Pauli, in 1930, to postulate the existence of a third, by then undetected particle involved in the process. The neutrino was predicted to be a very light, uncharged fermion, primarily proposed to account for missing quantities such as energy and momentum. Neutrinos from radioactive decays originate from either natural sources, such as Geo-neutrinos, or artificial sources, such as fission reactors, which were the basis for the first detection of neutrinos. Examples for experiments that make use of reactors to study neutrino properties are KamLAND or Daya Bay [4, 5].

Another important source for neutrino studies on Earth is the Sun. Here the produced neutrinos originate from nuclear fusion processes inside the Sun, mainly the proton-proton-chain

$$^4p \rightarrow {}^4_2\mathrm{He} + 2e^+ + 2\nu_e \tag{2.2}$$

where protons fuse together to form a Helium-nucleus while producing positrons and electron neutrinos. The first observation of solar neutrinos was done by the Homestake experiment [6]. Compared to theoretical predictions, the results of the experiment showed a deficit of observed solar neutrinos, which built the start of the solar neutrino problem. Subsequent experiments, including Sudbury Neutrino Observatory (SNO) and Super-Kamiokande (Super-K), could confirm these results and additionally provided evidence supporting the theory of neutrino oscillations [7, 8]. Although the deficit in electron neutrinos was still detected, the total measured neutrino flux including all flavors, had been in good agreement with the predictions. This has been the first compelling evidence that neutrinos can change their flavor, which is discussed in detail in 2.4.

In the following, attention is directed toward the two most important categories of neutrino sources for the IceCube Neutrino Observatory: atmospheric and astrophysical neutrinos.

2.1.1. Atmospheric Neutrinos

By atmospheric neutrinos, one commonly refers to neutrinos that are produced as secondary particles in interactions of cosmic cays (CRs) with Earth's atmosphere. CRs are high-energy charged particles, such as protons or heavier ionized atomic nuclei, propagating through the universe [9, 10]. Observing CRs has been an extensive field of research in astroparticle physics, by using different kinds of detectors and techniques to investigate the arriving particle flux over a large range of energies. The cosmic ray energy spectrum approximately follows an inverse power law

$$\frac{d\phi}{dE} = \frac{d^4N}{dE\,dA\,d\Omega\,dt} \sim E^{-\gamma} \tag{2.3}$$

which describes the differential particle flux of CRs per unit energy. It is mainly determined by the spectral index γ which varies over the total spectrum depending on the energy. The shape of the CR energy flux is given by 2.1 in a measured all-particle spectrum.

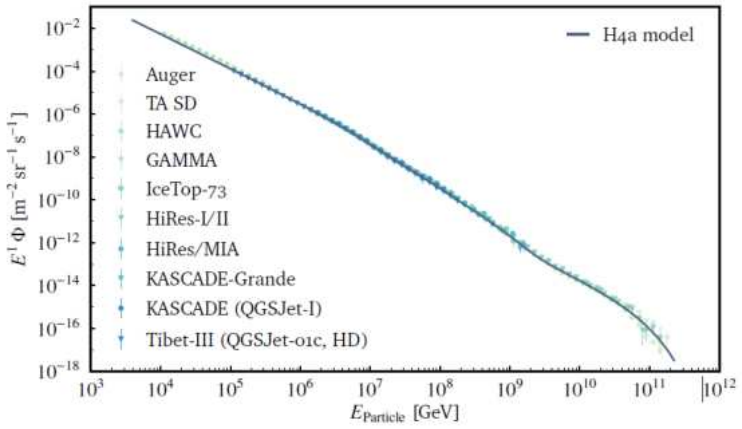

Figure 2.1.: All-particle high-energy cosmic ray spectrum as a function of particle energy. The plot shows the energy spectrum with data from various experiments [10].

As already noted, depending on the energy the spectrum shows distinct features. Thus the most prominent ones should be mentioned. Starting from an energy region of 10 GeV to 1 PeV that is described by the same power law dependence, the spectrum steepens in the region ranging from 10 PeV to 1 EeV. The transition of these two is located at around 3 PeV and is commonly referred to as the "knee". Passing another transition region at $\sim$ 3 EeV, known as the "ankle", the spectrum flattens again for energies above 10 EeV. For ultra-high energies above 10^{20} eV the spectrum appears to cut off. The reason for the latter is not clearly identified yet. Most likely it either reflects a maximum accelerating power of particles by astronomical objects or a potential dampening due to interactions with photons from the cosmic microwave background (CMB), also called the Greisen-Zatsepin-Kuzmin cutoff.
For the first transition region at the knee, it is believed that the contribution of galactic particle accelerators starts to decrease, resulting in a significant steepening of the flux spectrum. For even higher energies at the ankle galactic source contributions effectively die out, while extragalactic sources are postulated to recover this, leading to the re-flattened part of the spectrum [10–12].

Arriving at Earth, the CR-particles interact with ambient matter of the atmosphere and produce cascades of secondary particles, like pions, kaons and other hadrons. These secondary particles may induce the production of further ones by either decaying or interacting again with matter[1]. This interaction-/reaction-chain is called an extensive air shower and includes the production of (atmospheric) neutrinos. Typically these can be divided into two sub-categories: a conventional and a prompt neutrino flux. The conventional flux is mainly the result of decaying lighter mesons, such as pions and kaons

$$\pi^{\pm} \;\rightarrow\; \mu^{\pm} + \nu_{\mu}(\overline{\nu}_{\mu}) \tag{2.4}$$

$$K^{\pm} \;\rightarrow\; \mu^{\pm} + \nu_{\mu}(\overline{\nu}_{\mu}) \tag{2.5}$$

where the produced muons may further decay themeselves

$$\mu^{\pm} \;\rightarrow\; e^{\pm} + \nu_{e}(\overline{\nu}_{e}) + \overline{\nu}_{\mu}(\nu_{\mu}) \tag{2.6}$$

producing additional neutrinos.

The prompt flux, on the other hand, is the result of heavier meson and baryon decays with potential heavy-quark-contribution [10]. These quarks tend to quickly hadronize, forming amongst others charmed hadrons like D mesons, which directly

[1]These interactions include further hadronic but also electromagnetic processes via the production of photons etc.

produce neutrinos by rapidly decaying via either (semi-) leptonic or fully hadronic processes [13]. While the conventional flux dominates in the low-energy regime, the prompt flux is expected to become significant[2] above energies of roughly 10^6 - 10^7 GeV. Since these heavy intermediate hadrons have very short lifetimes and typically decay immediately, the prompt flux is expected to follow the primary cosmic ray spectrum. This is different to the case of the conventional flux, where the secondary particles traverse the atmosphere for a considerable amount of time and distance, while potentially losing energy, which makes this flux component dependent on the particle's energy and its incident angle, which eventually leads to a reduction at higher energies and an anisotropy of the flux [10].

Both, conventional and prompt flux, are modelled by a power law, just like the primary cosmic ray spectrum. The prompt neutrino flux is expected to closely follow the pimary CR-spectrum, whereas the contribution of the conventional flux in general shows a steeper behaviour due to potential energy losses[3] of the secondary particles along their path through the atmosphere.

Finally, the distinct production mechanisms further result in different flavor compositions. The conventional flux provides a flavor ratio $(\nu_e, \nu_\mu, \nu_\tau)$ of $(1 : 2 : 0)$ for its contribution at lower energies, while for higher energies this shifts to $(0 : 1 : 0)$ as the muon decay is less likely to happen. For the prompt flux, on the contrary, a ratio of $(1 : 1 : 0.1)$ is expected [15].

2.1.2. Astrophysical Neutrinos

On top of the atmospheric neutrino flux, a contribution of astrophysical neutrinos has been discovered by analyzing IceCube data. In 2013, IceCube presented its first evidence of an diffuse, high-energy component of astrophysical neutrinos in the total measured flux. Back then an analysis of data that covered two years from 2010 - 2012, respecting the reconstructed energies, arrival directions and event topologies, showed a significant excess of neutrino events in the range of 30 - 1200 TeV compared to what was expected from neutrinos originating only from atmospheric processes. It included neutrino events of all flavors, but the interaction vertices had to be contained within the instrumented volume of the IceCube detector [16].

A later analysis, based on six years data from 2009 - 2015, independently showed a significant astrophysical contribution and led to an exclusion of a purely atmospheric origin for the highest-energy neutrinos [17].

[2] This is mainly due to higher energies necessary to produce these heavy particles

[3] The different decay processes, given in 2.4-2.6, contributing to the conventional flux show different critical energies above which the respective production of neutrinos is significantly reduced [14].

The main results of the latter analysis are visualized in 2.2, where the astrophysical flux on top of the (conventional) atmospheric one can be nicely seen. The most recent results on the observation of the diffuse astrophysical neutrino flux show a flux normalization of $\phi_{Astro}^{per-flavor} = 1.68$ TeV (at 100 TeV) and a spectral index of $\gamma = 2.58$ for energies ranging from 3 TeV to 500 TeV.

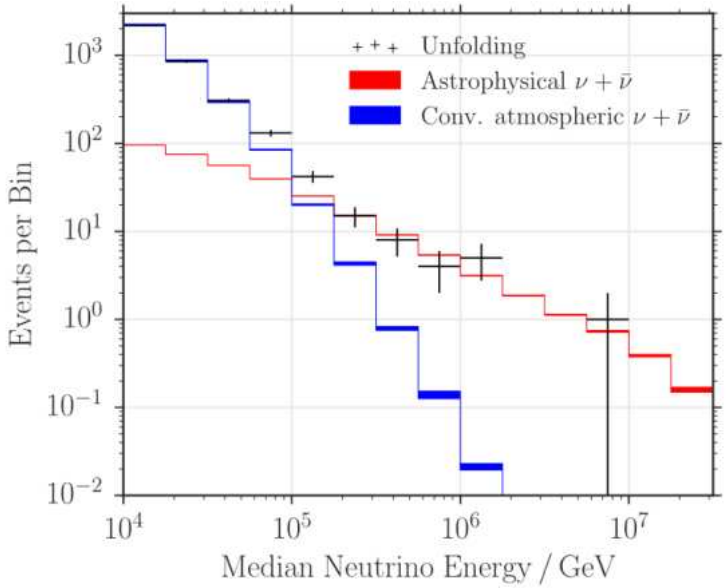

Figure 2.2.: Energy-dependent behaviour for the respective flux contributions, i.e. the conventional atmospheric and the astrophysical component, to the total measured neutrino flux. For a given range of energies, it displays the counts of neutrino events falling into a certain reconstructed energy bin for an analysis using up-going muon data from IceCube [17]. The blue and red curve show the models of conventional atmospheric and diffuse astrophysical component using the best-fit parameters to represent the true/experimental data, respectively. The black crosses correspond to the actual experimental data.

After identifying the diffuse astrophysical neutrino flux component, research has increasingly focused on locating (extra)galactic sources responsible for these high-energy neutrinos. Prominent candidates for such sources include supernovae, stellar fusion processes, interactions between ultra-high-energy cosmic rays and the interstellar medium, gamma-ray bursts (GRBs), or active galactic nuclei (AGNs).

Among these, the blazar TXS $0506 + 056$ stood out as a notable example. It has shown high statistical significance to portray a potential neutrino point source. A high-energy neutrino event detected by the IceCube Neutrino Observatory was spatially and temporally associated with a gamma-ray flare observed by Fermi-LAT. This coincidence not only highlights the progress in multi-messenger astronomy, but also provides compelling evidence to investigate such objects as potential neutrino sources [1, 18].

Additionally, in 2022, the active galaxy NGC 1068 could be identified as another neutrino source. The contrasting properties of TXS $0506 + 056$ and NGC 1068 suggest that multiple populations may contribute to the observed astrophysical neutrino flux [3].

Recent advancements in the search for neutrino sources include the observation of high-energy neutrinos from the Galactic plane. Due to the amount of matter that is expected and the fact that the Milky Way is one of the most prominent features visible in the gamma-ray flux, there had been good reason to investigate if an excess of high-energy neutrinos could be found. The analysis conducted for that showed significant evidence that the Galactic plane is indeed contributing a diffuse neutrino emission. However no further structure could be resolved [19].

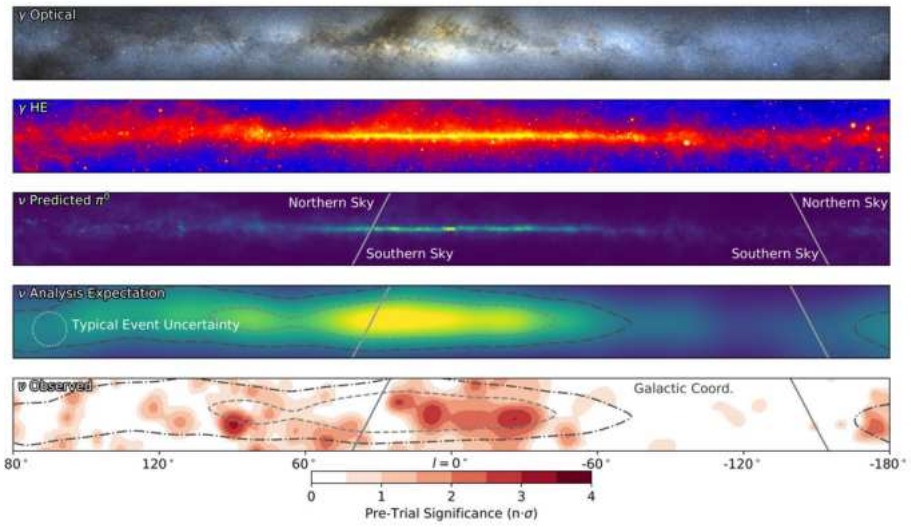

Figure 2.3.: A multi-messenger view of the Milky Way galaxy. Each panel shows the entire Galactic plane. The panels, from top to bottom, display: the view in the optical range, the integrated flux in gamma rays, the emission template for the expected neutrino flux, the emission template from the previous panel convolved with the IceCube detector acceptance and lastly pre-trial significance of the all-sky scan for point-like sources [20].

In general high-energy astrophysical neutrinos are expected to originate from hadronic processes like photo-nuclear

$$p\gamma \rightarrow \Delta^{+} \rightarrow \begin{cases} p\pi^{0} \\ n\pi^{+} \end{cases} \tag{2.7}$$

or proton-proton-collisions

$$pp \rightarrow \begin{cases} pp\pi^{0} \\ pn\pi^{+} \end{cases} \tag{2.8}$$

that are amongst the most important neutrino production mechansisms for astronomical objects by generating secondary decaying mesons[4].

2.2. Neutrinos in the Standard Model and Beyond

As the previous section already covered neutrino origins, including their sources and production mechanisms, and further examined key physical processes involving neutrinos, this section aims to delve deeper into the fundamental physics of neutrino particles, providing a more comprehensive understanding of their properties.

In the Standard Model (SM) of particle physics, neutrinos are described as uncharged massless fermions, that interact exclusively via the weak force. As leptons, neutrinos can be divided into three different generations:

$$\begin{pmatrix} \nu_e \\ e^- \end{pmatrix} \begin{pmatrix} \nu_\mu \\ \mu^- \end{pmatrix} \begin{pmatrix} \nu_\tau \\ \tau^- \end{pmatrix}$$

each containing a charged lepton and the corresponding neutrino as well as their respective antiparticles.

So far neutrinos have been observed exclusively in left-handed states, while antineutrinos have only been detected in right-handed states. Due to the absence of a right-handed component, the mass term $m_\nu(\overline{\nu_L}\nu_R + \overline{\nu_R}\nu_L)$ vanishes in the SM Lagrangian and the neutrino is predicted to have zero mass. Accordingly the neutrinos should travel at the speed of light and the helicity of being left- or right-handed should be conserved, respectively [21, 22].

Even though this is indeed observed in experiments, there has to be more to neutrino physics, even beyond the SM. This is highly motivated by the well established fact

[4] Eq. 2.4 gives an example of how this translates then further to neutrino production.

that neutrinos, in contrast to the prediction of the SM, are massive particles. Evidence for that is found in the observed effect of neutrino oscillations, where a neutrino that was initially produced in a particular flavor state shows a certain probability of changing its state while travelling away from the source, such that it may be detected in another flavor. The observation of neutrino oscillations is directly related to the fact that neutrinos have finite mass. Apart from the determination of the exact values, it is an active research how the mass is assigned to the particles. One of the most promising attempts is by assuming neutrinos as Majorana particles. By fulfilling the Majorana condition $\nu_R = C\,\overline{\nu}_L^T$ a mass term $\propto \frac{m_\nu}{2}\overline{\nu}_L\nu_L + h.c.$ that only explicitly contains left-handed neutrinos is included. This would further cause that the neutrino is its own antiparticle $\nu = \nu^C$, but could potentially solve some of the biggest still open questions, including the observed matter-antimatter asymmetry [9, 21, 23]. The most promising experimental approach to investigate this, is the search for Neutrinoless Double Beta Decays $0\nu\beta\beta$ using neutrino experiments like LEGEND [24]. Furthermore, this could naturally explain the small neutrino mass via the seesaw mechanism, which would involve the existence of a heavy, right-handed sterile neutrino [23, 25].

Despite of the fact that the SM has to be extended, experiments based on neutrino interactions have been in great agreement with its predictions. Hence, the following section discusses basic neutrino interactions.

2.3. Neutrino Interactions

In weak theory, neutrinos interact with other particles via either charged-current (CC) or neutral-current (NC) processes. These interactions are mediated by the $W^\pm$ and Z^0 boson, respectively and the corresponding Lagrangians[5] for processes where neutrino fields are involved read as

$$\mathcal{L}_{CC} = -\frac{g}{2\sqrt{2}}\, j_\mu^{CC}\, W^\mu \;+\; h.c. \tag{2.9}$$

$$\mathcal{L}_{NC} = -\frac{g}{2\cos\theta_W}\, j_\mu^{NC}\, Z^\mu \tag{2.10}$$

[5]Here g is the gauge coupling constant of the weak symmetry group and θ_W is the weak mixing angle.

with the charged and neutral currents

$$j_\mu^{CC} = \sum_\alpha \overline{\nu}_\alpha \gamma_\mu (1-\gamma^5) l_\alpha \ + ... \tag{2.11}$$

$$j_\mu^{NC} = \sum_\alpha \overline{\nu}_\alpha \gamma_\mu (1-\gamma^5) \nu_\alpha \ + ... \tag{2.12}$$

where $(1-\gamma^5)$ is basically responsible for the projection onto the left- and right-handed parts for particles and antiparticles, such that only the respective components contribute in weak interactions. For simplicity, the denoted Lagrangians and currents only explicitly contain expressions that include neutrino fields, respectively [10, 26]. The left part of figure 2.4 depicts the CC interaction vertex of neutrinos. Here the incoming neutrino is converted to the charged lepton of the associated flavor by emitting a $W^\pm$-boson. The right part analogously shows the NC interaction vertex, that is carried by the exchange of a Z^0-boson. The outgoing particle in that case is still a neutrino[6].

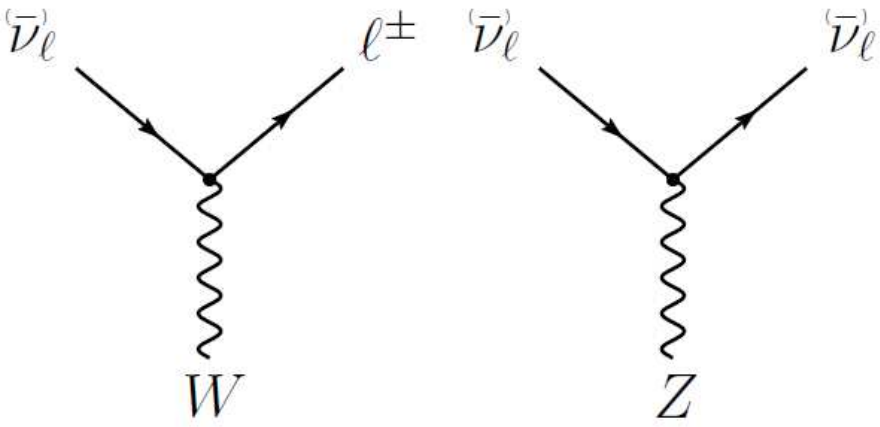

Figure 2.4.: Feynman diagrams of neutrino charged current (left) and neutral current (right) interactions [27]. Here the focus lies on the neutrino interaction vertices such that the interaction partners in the figure are omitted.

[6]Section 3.1 gives more complete picture of neutrino-nucleus interaction, including all interaction partners.

2.4. Neutrino Oscillations

As already mentioned, neutrinos oscillate in their flavor states. The effect of neutrino oscillations is directly associated to the fact that the flavor states are not equal to the energy-/mass-eigenstates.

In the following, neutrino oscillations are investigated by their transition probabilities for the simple case of only two flavor states for neutrinos propagating in vacuum, which is followed by an overview on the general all-flavor situation and an outline of matter effects on neutrino oscillations.

The flavor-basis may be expressed in terms of the energy-eigenstates via

$$\begin{pmatrix} |\nu_\alpha\rangle \\ |\nu_\beta\rangle \end{pmatrix} = \begin{pmatrix} \cos\theta & \sin\theta \\ -\sin\theta & \cos\theta \end{pmatrix} \cdot \begin{pmatrix} |\nu_1\rangle \\ |\nu_2\rangle \end{pmatrix}$$

where the entries of the matrix basically arise from common requirements to describe an unitary transformation, including the mixing angle θ as a free parameter.
Starting from the plane wave solutions[7] for the time evolution of the energy-eigenstates and assuming an initially pure $|\nu_\alpha(t=0)\rangle$ state[8], one finds

$$|\nu_\alpha(t)\rangle = \cos\theta\ e^{-iE_1 t}\,|\nu_1\rangle + \sin\theta\ e^{-iE_2 t}\,|\nu_2\rangle \tag{2.13}$$

for how the neutrino develops in time. By projecting this onto the other flavor state and taking the absolute square, one obtains the transition probability[9] as

$$P_{\nu_\alpha\to\nu_\beta}(t) = |\,\langle\nu_\beta \mid \nu_\alpha(t)\rangle\,|^2 = P_{\nu_\alpha\to\nu_\beta}(L) = \sin^2(2\theta)\,\sin^2\left(\frac{\Delta m^2_{21}}{4E}L\right) \tag{2.14}$$

with the squared mass difference $\Delta m^2_{21} = m_2^2 - m_1^2$, the neutrino energy E and L as the distance travelled by the particle from its production site to its current position. To derive this explicit term, the relativistic limit of $m_i << |\vec{p}|$ was used to approximate the energy $E_i = \sqrt{\vec{p}^2 + m_i^2} \approx E + \frac{m_i^2}{2E}$ using equal definite momenta $\vec{p}_i = \vec{p}$, setting $E := |\vec{p}|$ and further assuming that the neutrinos approximately move at the speed of light $v \approx c$. In 2.5 the situation for this simplified two-flavor vacuum case is shown by displaying the derived transition probabilities in dependence on the travel distance.

[7] The used plane waves solve the time-dependent part of the free Hamiltonian.
[8] $|\nu_\alpha(t)\rangle$ is the time-dependent state of the neutrino that was initially prepared in the α-flavor state.
[9] Here and in the following using natural units, i.e. $c = 1$ and $\hbar = 1$ etc.

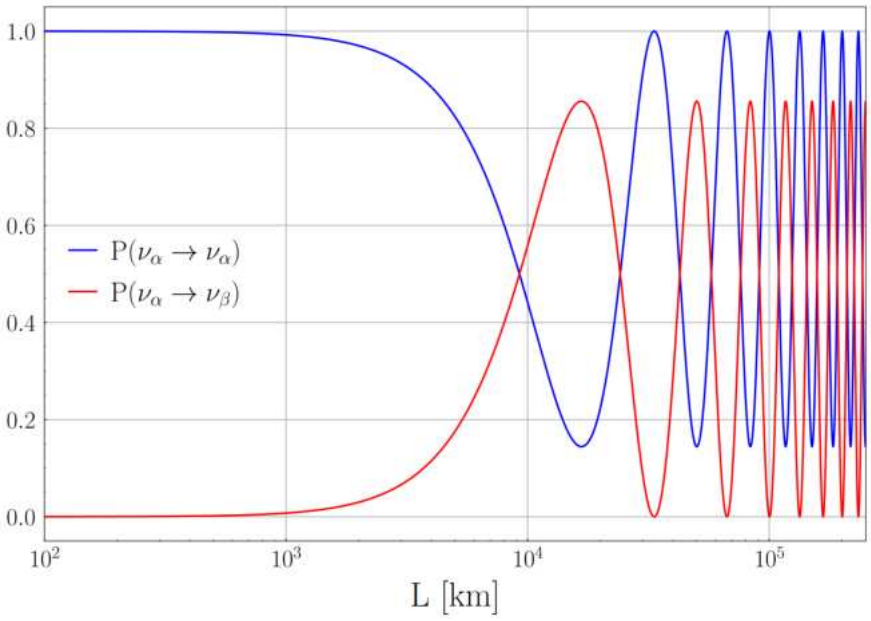

Figure 2.5.: Transition probabilities due to neutrino oscillations, depending on the travelled distance, in the simplified two-flavor case for a neutrino that was initially prepared in the $|\nu_\alpha\rangle$ state. The probability to find the particle in the $|\nu_\beta\rangle$ state $P(\nu_\alpha \to \nu_\beta)$ is given by eq. 2.14 and the probability to still find the neutrino in its initial state is correspondingly $P(\nu_\alpha \to \nu_\alpha) = 1 - P(\nu_\alpha \to \nu_\beta)$. The plot is based on example values of $\theta = 0.59$, $\Delta m^2_{21} = 7.42 \cdot 10^{-5}$ eV^2 and $E = 1$ GeV.

Transferring this into the more general picture that includes all (known) neutrino flavors we find

$$\begin{pmatrix} |\nu_e\rangle \\ |\nu_\mu\rangle \\ |\nu_\tau\rangle \end{pmatrix} = \begin{pmatrix} U_{e1} & U_{e2} & U_{e3} \\ U_{\mu 1} & U_{\mu 2} & U_{\mu 3} \\ U_{\tau 1} & U_{\tau 2} & U_{\tau 3} \end{pmatrix} \cdot \begin{pmatrix} |\nu_1\rangle \\ |\nu_2\rangle \\ |\nu_3\rangle \end{pmatrix}$$

where

$$U = \begin{pmatrix} 1 & 0 & 0 \\ 0 & c_{23} & s_{23} \\ 0 & -s_{23} & c_{23} \end{pmatrix} \begin{pmatrix} c_{13} & 0 & s_{13}e^{-i\delta} \\ 0 & 1 & 0 \\ -s_{13}e^{i\delta} & 0 & c_{13} \end{pmatrix} \begin{pmatrix} c_{12} & s_{12} & 0 \\ -s_{12} & c_{12} & 0 \\ 0 & 0 & 1 \end{pmatrix}$$

describes the unitary transformation between mass- and flavor-basis, and is called the Pontecorvo–Maki–Nakagawa–Sakata (PMNS) matrix [28, 29]. If neutrinos are in fact Majorana particles the matrix would have to be expanded by multiplying another

matrix to the right in the definition of the PMNS matrix above, introducing two more complex phases as free parameters. But since these phases do not alter observables of neutrino oscillations they can be omitted anyways in the following [10, 30]. In the used notation s_{ij} and c_{ij} denote $\sin\theta_{ij}$ and $\cos\theta_{ij}$, respectively. The complex phase δ is besides the three mixing angles θ_{ij} the fourth free parameter of the PMNS matrix and accounts for a potential CP-violation which would manifest in a different oscillatory behaviour for particles and antiparticles respectively, i.e. $P(\nu_\alpha \to \nu_\beta) \neq P(\overline{\nu}_\alpha \to \overline{\nu}_\beta)$, which is a common requirement to explain the matter-antimatter asymmetry via leptogenesis [30, 31]. A further property that is to be tested is the unitarity of the matrix. An observed deviation of it would directly lead towards new physics which would have to be solved by e.g. including sterile neutrinos as a further dimension.
From analogue considerations as done in 2.13-2.14, the transition probabilities may be calculated as

$$\begin{aligned} P_{\nu_\alpha \to \nu_\beta}(L) &= \left| \sum_{i=1}^{3} U_{\beta i} \exp\left(-i \frac{m_i^2 L}{2E}\right) U_{\alpha i}^* \right|^2 \\ &= \delta_{\alpha\beta} - 4 \sum_{i<j} \mathrm{Re}\left(U_{\alpha i}^* U_{\beta i} U_{\alpha j} U_{\beta j}^*\right) \sin^2\left(\frac{\Delta m_{ij}^2 L}{4E}\right) \\ &\quad + 2 \sum_{i<j} \mathrm{Im}\left(U_{\alpha i}^* U_{\beta i} U_{\alpha j} U_{\beta j}^*\right) \sin\left(\frac{\Delta m_{ij}^2 L}{2E}\right) \end{aligned} \tag{2.15}$$

As all previous considerations were based on the assumption of a vacuum environment, it should be noted that the dynamics have to be adjusted for the case when neutrinos travel through matter. The presence of electrons and nucleons in regular matter influences neutrino oscillations by extending the effective Hamiltonian $H = H_0 + V$ in the flavor-basis

$$i \frac{\partial}{\partial t} \begin{pmatrix} \nu_e \\ \nu_\mu \\ \nu_\tau \end{pmatrix} = \left[\frac{1}{2E} U \begin{pmatrix} m_1^2 & 0 & 0 \\ 0 & m_2^2 & 0 \\ 0 & 0 & m_3^2 \end{pmatrix} U^\dagger + \begin{pmatrix} V & 0 & 0 \\ 0 & 0 & 0 \\ 0 & 0 & 0 \end{pmatrix} \right] \begin{pmatrix} \nu_e \\ \nu_\mu \\ \nu_\tau \end{pmatrix} \tag{2.16}$$

where $V = \sqrt{2} G_F n_e$ is the effective matter potential with the Fermi coupling constant G_F and the electron density n_e of the ambient matter.
Again working in a basic two-flavor approximation, analogously to 2.14 with only ν_e and ν_μ, but now based on the effective Hamiltonian, one finds that the transition probability scales with

$$P_{\nu_e \to \nu_\mu}(L) \propto \frac{\left(\frac{\Delta m^2}{4E}\right)^2 \sin^2 2\theta}{\left(\frac{\Delta m^2}{4E} \cos 2\theta - \sqrt{2} G_F n_e\right)^2 + \left(\frac{\Delta m^2}{4E}\right)^2 \sin^2 2\theta} \tag{2.17}$$

which hosts a possible resonant mixing amplification when $\sqrt{2}G_F n_e = \frac{\Delta m^2}{4E} \cos 2\theta$, also called the Mikheyev- Smirnow-Wolfenstein (MSW) resonance.
Thus, one of the main results of matter effects in neutrino oscillations is that even for small mixing in vacuum it may be large in matter. The basic difference in matter arises from the fact that the energy-eigenstates and the corresponding dynamics are altered with respect to the vacuum case. Furthermore, since the sign of the potential V in eq. 2.16 flips for antineutrinos, this effect acts differently for neutrinos and antineutrinos. This broken particle-antiparticle degeneracy of the MSW-effect eventually allowed the determination of the sign for the solar mass splitting Δm^2_{21} to be positive [10, 32, 33].

In general, studying the effect of neutrino oscillations requires knowledge on the initial flavor composition of the neutrino flux that should be measured. For experiments that detect neutrinos from artificial sources, like reactors, this is realized by placing a second detector near the source. Comparing the flavor compositions of the initial flux and the one that is measured by the detector farther away, allows to determine neutrino mixing parameters.

However, for neutrino telescopes, like IceCube, this is not really feasible. Neutrino oscillation studies in IceCube are primarily based on atmospheric neutrinos. Since comic rays and their interactions in Earth's atmosphere have been studied thoroughly, the initial neutrino flux can be modelled with good precision. Hence, the measurement of the flavor composition that arrives at IceCube at the South Pole provides a way to determine mixing parameters with atmospheric neutrinos. The latest result of atmospheric neutrino oscillation studies using IceCube DeepCore[10] data measured $\Delta m^2_{32} = 2.40\ ^{+0.05}_{-0.04} \cdot 10^{-3}$ eV^2 and $\sin^2\theta_{23} = 0.54\ ^{+0.03}_{-0.03}$. The results are the most precise to date using atmospheric neutrinos and are compatible with measurements from other neutrino detectors, including long-baseline accelerator experiments [34].
In principle this can be done as well for astrophysical neutrinos, but due to the strong model-dependence and the large travel distances this is a rather difficult task. For astrophysical neutrinos, IceCube so far has measured an averaged effect of neutrino mixing.

[10] see chapter 3 for a more detailed description of the IceCube detector

The following table 2.1 gives a complete overview of the current knowledge on neutrino mixing parameters, based on data from several experiments.

Parameter	**Unit**	**Best fit (90% CL)**	
		NH	IH
Δm^2_{21}	10^{-5} eV^2	7.53 ± 0.18	
$\lvert\Delta m^2_{32}\rvert$	10^{-3} eV^2	2.45 ± 0.03	2.54 ± 0.03
$\sin^2\theta_{12}$	10^{-1}	3.07 ± 0.13	
$\sin^2\theta_{23}$	10^{-1}	5.46 ± 0.21	5.39 ± 0.22
$\sin^2\theta_{13}$	10^{-2}	2.20 ± 0.07	
δ	π	$1.36^{+0.20}_{-0.16}$	

Table 2.1.: Current knowledge of neutrino mixing parameters given as the 90% confidence levels for both normal (NH) and inverted (IH) hierarchies. NH is referring to the case that m_3 is the largest mass while for IH m_3 is the smallest one. The difference of the two scenarios would have great impact on the measurement of the total neutrino mass. The table is based on rounded data from [35].

3. IceCube Neutrino Observatory

The IceCube Neutrino Observatory is a large volume neutrino telescope placed at the South Pole and located near the Amundsen-Scott South Pole Station. In a depth of 1450m − 2450m, it uses one cubic kilometer of Antarctic ice as optical medium to detect neutrinos. The detector is placed at significant depth below the surface to shield against cosmic rays and their secondary particles. The large volume of the detector is typical for neutrino experiments. It is necessary to counteract the small cross section to detect these elusive particles at a sufficient rate and to ensure that the typically large signals are contained inside the detector. The In-Ice array of IceCube currently hosts 86 strings with 60 digital optical modules (DOMs) each, equipped with a PMT detecting Cherenkov photons generated by secondary particles that are produced in neutrino interactions and traverse the detector volume. The neutrino's energy and arrival direction is reconstructed by measuring the amount of light and monitoring the arrival time at different modules. The electrical connections of the modules provide the necessary power supply and DAQ system for the detector.

The main part of the IceCube detector, consists of 78 strings arranged on a hexagonal grid with an average horizontal spacing of 125 m and a vertical separation of 17 m for the attached DOMs. The spacing between the sensors together with the used trigger techniques lead to a neutrino detection energy threshold of approximately 100 GeV [27].

At the center, 8 strings were deployed more compactly with a string spacing of 70 m and a vertical DOM separation of 7 m, respectively. This inner part of the detector is called DeepCore and was included to lower the energy threshold down to approximately 5 GeV and improve the directional and energy resolution. The increased detector sensitivity in this region allows to study effects like neutrino oscillations [27].

Furthermore, 81 stations each hosting two tanks equipped with downward facing DOMs are placed on top of the strings. This part is called IceTop and is mainly used as a veto detector and to study cosmic ray physics.

The detector, fully operating since 2011, is primarily designed to observe astrophysical neutrinos. The most important results of IceCube studies so far include the discovery of the astrophysical neutrino flux component and the first evidence for identifying neutrino point sources [1, 3, 36].

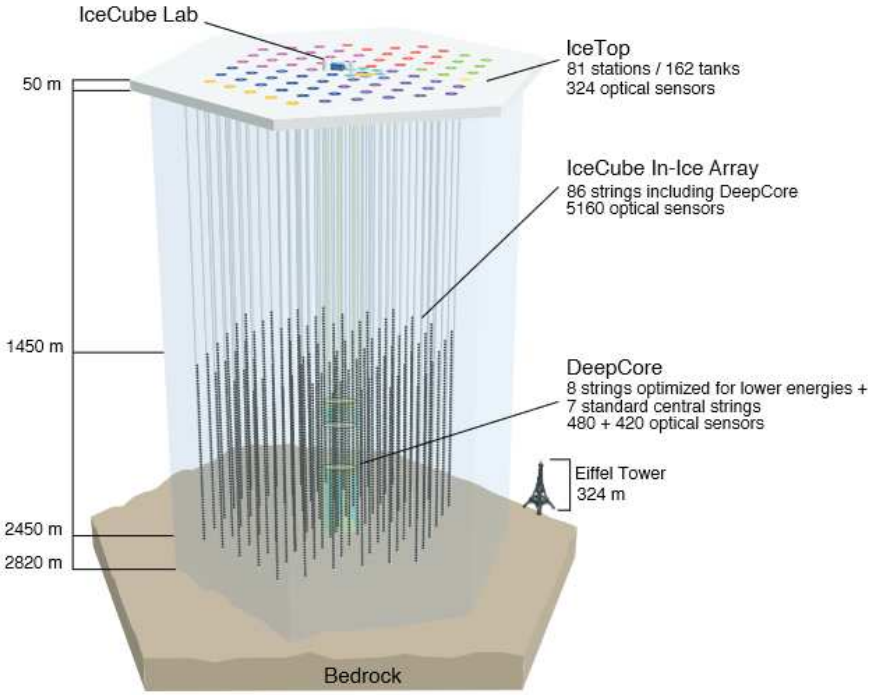

Figure 3.1.: Schematic illustration of the IceCube detector layout with its main four sub-components, the IceCube Lab, IceTop, the IceCube In-Ice Array and DeepCore [37].

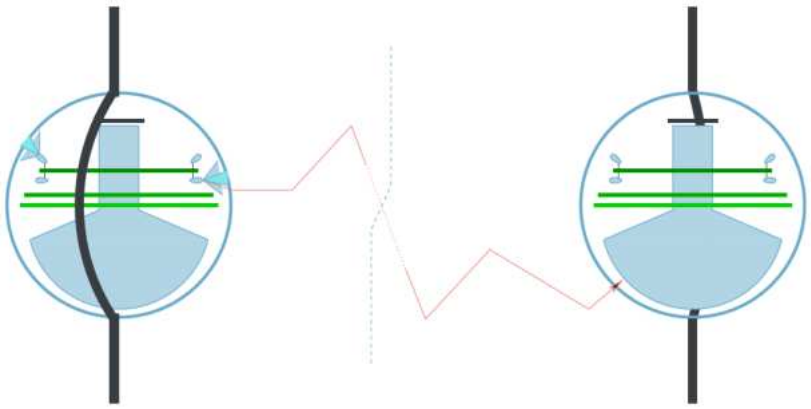

Figure 3.2.: Schematics of two DOMs as used in the detector. The LED of the left DOM emits light (red) that traverses the ice and is detected by the other module as it is done for current calibrations in IceCube [10].

3.1. Detection Principle

High-energy neutrino experiments, like IceCube, aim to detect neutrino-induced secondary leptons from charged current processes and other secondary particles produced by neutrinos scattering inelastically with the target material[1]. The leading process is deep inelastic scattering in charged or neutral current neutrino interactions with the target material

$$\nu_\alpha + N \rightarrow l_\alpha + X \quad \text{(CC)} \tag{3.1}$$

$$\nu_\alpha + N \rightarrow \nu_\alpha + X \quad \text{(NC)} \tag{3.2}$$

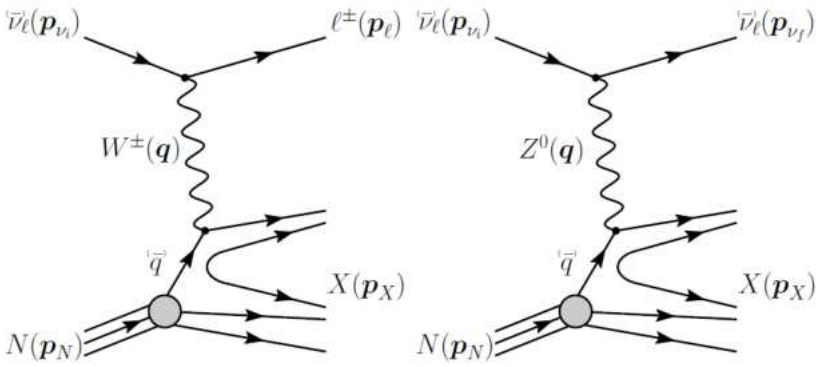

Figure 3.3.: Feynman diagrams for neutrino-nucleon deep inelastic scattering (DIS) via charged (left) and neutral (right) currents. An initial nucleon is denoted as N, and resulting hadrons are labelled by X [27].

Above energies of around 5 - 8 GeV the scattering is typically deep inelastic where the momentum transfer is large enough to disintegrate the nucleus and the neutrino interacts directly with quarks producing a hadronic shower. Additionally, in CC-processes a charged lepton is produced, whereas for NC-processes one of the outgoing particles is still a neutrino. The produced hadronic shower will further develop an electromagnetic component via stochastic processes like bremsstrahlung which will leave a signal in the detector as well[10, 27, 38, 39].

[1]The target material in IceCube mainly encompasses the hydrogen and oxygen nuclei

Charged particles traversing the detector medium at very high velocities may induce light emission due to the Cherenkov effect which is the main detection mechanism in IceCube. The Cherenkov effect describes the coherent emission of photons via the relaxation of electromagnetic polarization of the atoms and molecules contained in the detector medium caused by a charged particle that travels through it at velocities v faster than the associated speed of light $c_n = c/n$ inside the medium[2]. The emission of such plane waves along the particle's path characteristically results in a Cherenkov cone. A schematic illustration for that is given in 3.4.

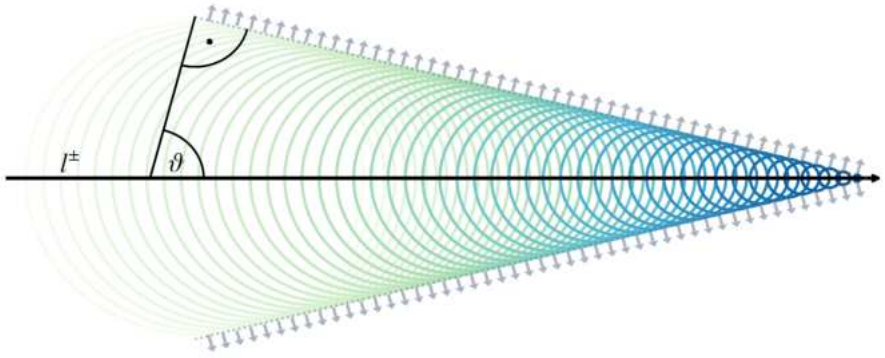

Figure 3.4.: Schematic illustration of the Cherenkov cone for a charged lepton $l^{\pm}$ traversing a dielectric medium from left to right at a velocity faster than the associated speed of light inside the medium [10].

The characteristic emission angle ϑ for that is given by $cos\vartheta = (\beta n)^{-1}, \beta = \frac{v}{c}$. For optically translucent media like ice, with a refractive index of $n \approx 1.3$, a highly relativistic particle $\beta \approx 1$ emits Cherenkov light under $\vartheta = 41^{\circ}$ [10]. The number N of Cherenkov photons generated per distance x and wavelength λ can be described analytically by the Frank-Tamm formula [10, 40]

$$\frac{d^2N}{dxd\lambda} = \frac{2\pi\alpha z^2}{\lambda^2}\left(1 - \frac{1}{\beta^2 n(\lambda)^2}\right) \tag{3.3}$$

where z is the electric charge of the particle and α the fine structure constant. The equation explains further why the Cherenkov light appears mostly blue, as more photons are produced for shorter wavelengths. Accordingly the detection of photons in IceCube is focussed on a wavelength regime of around 300-650 nm [27]. In this wavelength range, based on the values above, one would expect approximately 16,000

[2] n is the refractive index of the dielectric medium.

Cherenkov photons to be emitted for each meter the particle travels through the medium.

Finally, neutrinos of different flavors produce different signals for CC-process inside the detector which may result in the ability to gain further information on the particles. One can distinguish three basic event topologies: Cacade-like, Track-like and Double Bang events.

Cascade-like events happen when most of the neutrino's energy is deposited within a small region around the interaction vertex which leads to a spatially clustered light emission. They appear for either NC-processes for all flavors or CC-process where an electron neutrino is involved. Apart from the hadronic cascade the latter one produces an electron which may further interact with the ambient matter. However, due to its small maximum travel distance in ice, these events are nearly spherically shaped [10, 27].

Track-like events are mainly caused by muons that are produced in CC-processes either inside the detector (starting tracks) or outside (through-going). Due to the higher mass of the muon, the stochastic energy loss is decreased compared to electrons which results in typically larger travel distances. Thus a muon signal appears as a Cherenkov track inside the detector[10, 27].

Lastly, Double Bang events refer to signals that are caused by tau neutrinos. Due to their even higher mass, tau leptons are only affected by energy loss via ionization while travelling through the detector. However these particles have a very short lifetime, such that after their production at the interaction vertex they may only leave a short track of Cherenkov radiation followed by a second hadronic cascade due to the decaying process [10, 27].

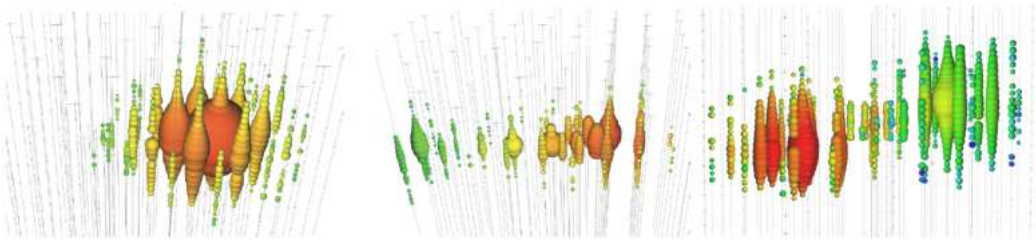

(a) *Cascade* (b) *Track* (c) *Double bang*

Figure 3.5.: Different IceCube neutrino signatures depending on the neutrino flavor. The figures show the sensor modules (dots) with size representing detected amount of light and color its arrival time [10].

3.2. Systematic Detector Effects

Studying neutrino physics with large volume experiments, like IceCube, inevitably entails systematic uncertainties that are of different origin. The Antarctic ice used as optical medium determines the the propagation of Cherenkov light which is produced by secondary particles from neutrino induced interactions and is eventually detected by the optical modules. The modules themselves strongly influence the effective signal by their detection characteristics such as their angular or wavelength dependent acceptance. But also the detector geometry and the background are contributing to how a neutrino signal looks like in the detector.

Thus it is important to calibrate the detector. The main focus here lies on the optical parameters[3] like absorption and scattering length, l_a and l_b, as well as the average scattering angle $\langle \cos\theta \rangle$. In a basic picture the emitted Cherenkov photons may either be scattered and change direction or be absorbed and are not detectable anymore [10]. The probabilities for the respective process result from a generalized Lambert-Beer law. The number of non-absorbed (non-scattered) photons given an inital number N_0 and after travelling the distance d inside the medium is

$$N(d) = N_0 \, e^{-d/l_{a,b}} \tag{3.4}$$

In general absorption and scattering limit the total amount of detected light and its directional propagation, which typically results in a decreased reconstruction precision.

Concerning the dominant systematics, the detector medium in IceCube may be divided into bulk and hole ice. The bulk ice covers the main part of the detector volume and determines the large scale propagation of photons by its depth-dependent absorption and scattering lengths, anisotropies and other effects like tilts of ice layers. Typical values[4] for bulk ice parameters[5] are $l_a > 100$ m, $l_b^{eff} \sim$ 30-40 m and $\langle \cos\theta \rangle \approx 0.95$ which are primarily driven by dust concentrations in the ice [10]. The hole ice is referring to the refrozen ice in the drill holes after deployment. It has been found that it contains high concentrations of air bubbles and affects the detector signal as it surrounds the optical modules [10, 27] .

[3] In theory the scattering of photons in ice can be described by Mie scattering.

[4] The values are given for relevant depths for the IceCube Upgrade and POCAM at around 2.2-2.5 km.

[5] Using the effective scattering length $l_b^{eff} = \frac{l_b}{1-\langle \cos\theta \rangle}$.

Figure 3.6.: Photos of a drill hole for a string deployment right before refreezing (left) and how the cloudy hole ice (right) looks like after has frozen again.

In both cases the associated ice parameters are obtained by comparing the results of calibration measurements with light emission simulations. For the calibration of the hole ice parameters two different approaches may be used: by either direct simulation or by shifting the problem to an effective acceptance of the optical modules [10].

Ultimately, after light has traveled through the ice, it may reach one of the optical modules. The DOM's response is influenced by the effective optical properties of its components, including quantum efficiencies, angular acceptances, and linearity with respect to incident photon fluxes, but also by the subsequent read-out electronics. Furthermore, the geometry of the detector and its modules is critical for accurately interpreting and reconstructing neutrino events, making it essential to determine the exact positions and potential tilts of the modules with the highest possible precision.

While the increasing number of neutrino events that are detected in IceCube progressively reduces statistical uncertainties, the systematic uncertainties are unbothered by that and become the dominant limit for reconstructions and data analyses. Acquiring more precise knowledge of ice parameters and optical module responses, is expected to significantly enhance the reconstruction performances and the detector's sensitivity to physics parameters. Hence, advanced optical modules and new calibration devices, including the Precision Optical Calibration Module, will be deployed in the context of the IceCube Upgrade to determine detector systematics with good precision.

3.3. IceCube Upgrade

The IceCube Upgrade is the first extension of the detector that will improve IceCube's scientific capabilities towards lower energies and neutrino oscillations by instrumenting an even denser region within DeepCore with seven additional strings.

The Upgrade strings will host around 700 new photosensor modules, namely the multi-PMT Digital Optical Module (mDOM) and the Dual optical sensors in an Ellipsoid Glass for Gen2 (D-Egg), with an inter-string and inter-module spacing of approximately 20 m and 3 m, respectively [41, 42]. Apart from optical modules, advanced calibration devices will be deployed. The new calibration devices encompass camera systems, acoustic positioning systems as well as calibration light sources. Among others this includes the Precision Optical Calibration Module (POCAM) [43, 44].

Figure 3.7 shows the preliminary deployment plan for the seven new strings in the context of the IceCube Upgrade with respect to the positions of the yet existing strings in the vicinity of DeepCore. The strings will be deployed in the 2025/26 South Pole working season and will include 21 POCAM devices in total.

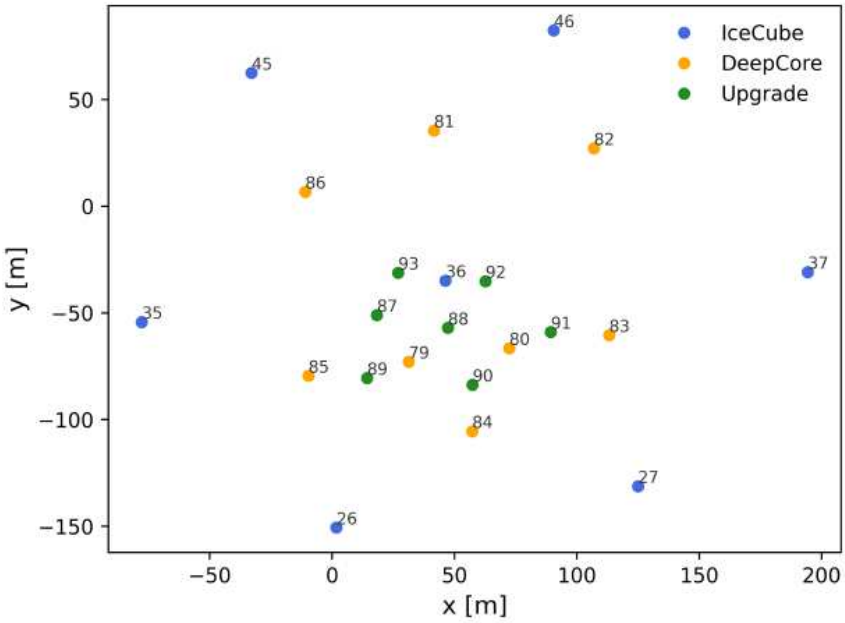

Figure 3.7.: Preliminary position of each IceCube-Upgrade string (green) relative to the existing IceCube (blue) and DeepCore (orange) strings.

The depth layout of the new devices can be divided into three regions. In the top area between 1350 m and 1850 m the IceCube-Upgrade strings are populated with a device spacing of 25 m on each string. Similar to the Deep Core strings this is followed by the so-called dust layer between 1850 m and 2150 m. Due to its worse optical properties this region is only sparsely instrumented. Most of the devices are located in the physics volume between 2150 m and 2450 m with a device-to-device separation of 3 m. In contrast to the IceCube and DeepCore, four of the IceCube Upgrade strings will be

instrumented in depths even below 2450 m. The devices will be placed between 2500 m and 2600 m and are planned to be used for studies of deep ice properties. The devices encompass, among others, mDOMs and D-Eggs as well as 7 POCAMs. Figure 3.8 gives an overview of the entire IceCube-Upgrade string layout.

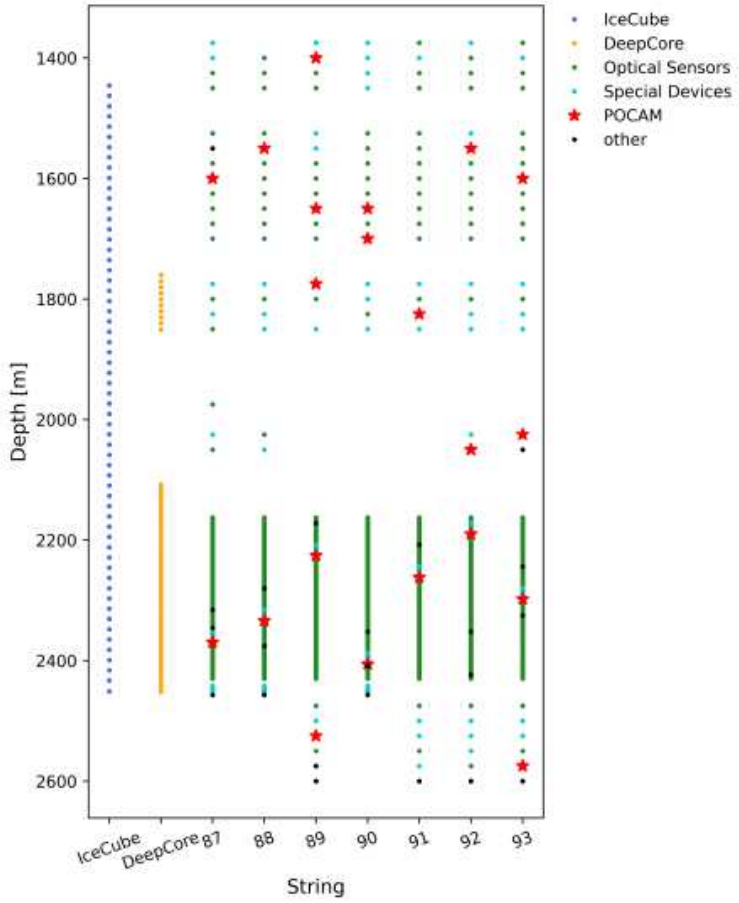

Figure 3.8.: Depth position of all the IceCube-Upgrade devices compared to the IceCube and DeepCore strings. IceCube modules are depicted in blue, Deep-Core in orange. The IceCube-Upgrade optical modules mDOM and D-Egg are shown in green, the special devices in light blue, and the POCAMs in red.

4. Precision Optical Calibration Module (POCAM)

Before finally dedicating to the characterization procedure of the Precision Optical Calibration Module (POCAM) in the next chapter, which covers the main work for this thesis, this chapter gives an overview on the POCAM device itself. This includes the general physical concept and motivation for the development as well as the final device design and its main components.

Figure 4.1.: Fully assembled POCAM device mounted into the harness by which it will be attached to the deployment strings via steel ropes. Beneath the glass hemisphere the diffusing sphere can be seen which is mounted onto a coated surface and is responsible for an isotropic light emission.

4.1. Physical Concept and Motivation

So far optical calibrations in IceCube had been carried out with the existing IceCube LED flashers (see 3.2). However these are limited by their intensity fluctuations as well as pointing accuracy which inevitably affects the calibration precision and eventually the detector sensitivity [10, 45]. To overcome this, POCAM has been developed. It is an characterized, isotropic and self-monitoring calibration light source. The precise knowledge on the flasher data like the angular emission profile, emission intensities, as well as spectral distributions and time profiles will contribute to an improvement compared to previous calibration methods.

POCAM hosts several emitters that can emit pulsed light flashes at different wavelengths optimized for the most relevant spectral parts of Cherenkov emissions in ice. Since the emission intensity is thoroughly investigated and by adding the ability to monitor itself in-situ, POCAM provides an improvement compared to the existing calibrations which only show an intensity precision of around 20 - 30 % [10]. Besides a general increased precision in calibrations, this will further provide the ability to include "bright" signals that typically had to be excluded from IceCube analyses so far due to rather poorly known linear behaviour of the optical modules. Likewise, as POCAM is developed as an isotropic light source, the problem of the pointing accuracy is removed as far as possible. Furthermore the short ($\sim$ ns) pulses will allow for a better time reconstruction of the signals produced in calibration procedures using POCAM. Here, self-monitoring not only gives a way to measure the emitted light intensity, but also track the flashing on a time basis.

The devices are designed to contain the current IceCube default wavelength of 405 nm and further emitters, such that a range of 350 - 530 nm is covered and the existing wavelength-dependent power-law behaviour may be verified [10, 45]. Lastly, the self-monitoring sensors cover a dynamic range to be able to properly track the behaviour for all different settings of intensities, pulse widths and wavelengths selectable for POCAM.

4.2. Device Design

The POCAM on the outside consists of two glass hemispheres where the emitted light passes through and a cylindrical pressure housing which contains the necessary electrical components. The instrument housing is mainly made from titanium and hosts a vacuum port for evacuation and nitrogen flushing purposes as well as a penetrator providing electrical connection to the device.

The main electrical components of POCAM consist of several circuit boards and may be divided into three subcategories: digital, interface and analog electronics.

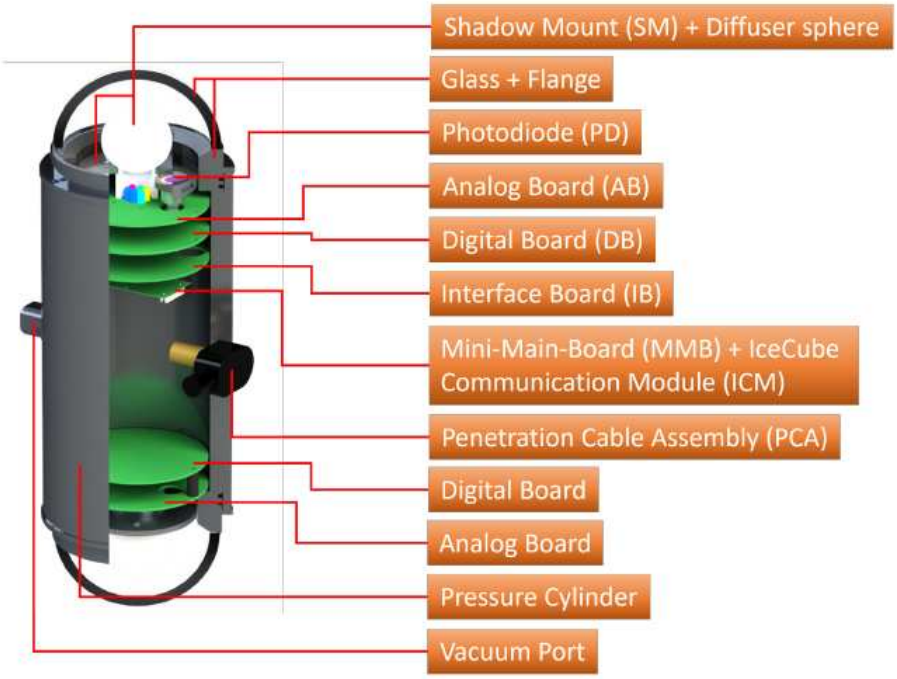

Figure 4.2.: The figure is a schematic cross-section of the POCAM showing its internal (electrical) structure. Figure taken from [10].

The interface electronics comprise the mini-main board (MMB) as well as the interface board (IB) that is specifically designed for POCAM. The MMB is actually a stack of three single boards which is developed by the IceCube collaboration and is used once within all devices to provide a homogeneous and standardized communication interface. One board of it mainly deals with power conversion for subsequent devices. Another board hosts the IceCube Upgrade microcontroller (MCU) as well as additional auxiliar sensors like accelerometers and magnetic field sensors to monitor the device's

orientation and potential tilt. The last board of the stack is the IceCube communication module (ICM) which provides necessary hard- and firmware to disentangle IceCube communication and time synchronization signals modulated on the power supply wire pair. Accordingly, in the context of POCAM, the most relevant capabilities of the MMB are its communication interfaces, the provided clock, trigger and synchronization signals as well as the provided baseline voltage [10].

Figure 4.3.: Mini-main board (MMB) stack, with the board dealing with power conversion on top, the control board at the bottom and the ICM connecting both in the middle.

The subsequent board to the MMB is the interface board. It is installed once per device and interfaces to both hemispheres independently via multi-strand teflon cables. One of its main functionalities is the generation of all required voltages in POCAM The circuits generating the high voltages exist twice per IB for redundancy and set voltages up to ~ 32 V, which eventually are applied to the analog electronics. Further the IB hosts the central trigger distribution system as it receives the external trigger and synchronization signals from the MMB. These signals are used to send out centralized and synchronous triggers to the digital boards [10].

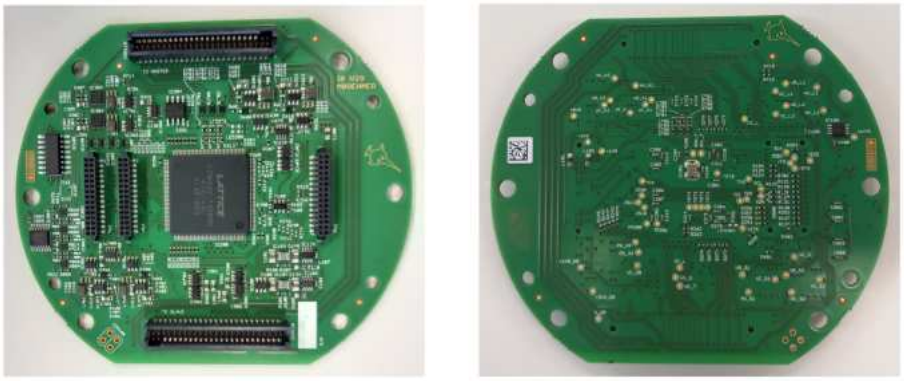

Figure 4.4.: Top (left) and bottom (right) view of the interface board (IB).

The digital board (DB) is the primary control board. It is directly connected to the analog and interface board and is installed once per hemisphere. The DB processes and distributes the signals, it receives from the interface board, to the analog board. It uses a variety of logical switching components, all controlled by a central FPGA-chip, providing the basic flashing configurations. This includes the correct pulse settings, like the emitter selection and intensity or pulse width configurations. Lastly, the DB hosts several sensors and an industrial-grade SD-card for temporary storage of the self-monitoring data [10, 45].

Figure 4.5.: Top (left) and bottom (right) view of the digital board (DB).

The final board that completes the main electrical components of POCAM is the analog board (AB). It is installed once per hemisphere and hosts the six light emitters, the respective pulse drivers to flash them as well as the self-monitoring sensors. The emitter matrix includes three light-emitting diodes (LEDs) and three laser diodes (LDs), enabling light emission at five different nominal wavelengths, 365, 405, 450, 465 and 520 nm which cover the most important spectral range for Cherenkov detectors like IceCube. As previously discussed, the main range is around 300 - 600 nm, while the the largest impact for IceCube physics is expected at shorter wavelengths. For the Icecube default wavelength 405 nm two emitters were included, of which one is a LED and the other one a LD. They are based on two distinct pulse drivers, the dual-configuration Kapustinsky driver and the LD-type driver.

In total two emitters, the LED of the just mentioned 405 nm ones and the LED flashing at 465 nm, make use of the Kapustinksy driver. For these emitters two distinct pulse driver configurations are available. Commonly referred to as “default” and “fast” mode, resulting in a nominal and a shorter pulse width.Applying a variable bias voltage to charge up a capacitor bank allows to achieve different the emission intensities.

The remaining four emitters were equipped with the LD-type driver. It uses existing technology for pulsing infrared laser diodes, adapted to the emitters in the spectral range of POCAM. Here, again a variable bias voltage of up to 32 V may be set that controls the emission intensity. An ultra-fast switching component, the LMG1020 allows for a multitude of driver pulse lengths such that many different widths for the emitted light pulses are selectable. Technically, this is realized by adjusting phase-shifts of the generated enable and disable trigger signals that set the driver pulse length by their relative delay. The trigger signals are generated on the FPGA of the digital board and are fed to the pulse driver on the AB to initiate (enable) and accordingly end (disable) the light emission. Besides variably setting the pulse width down to a few ns, LD-type drivers allow flashing at higher intensities compared to the Kapustinsky-drivers. For both pulse drivers two discharge paths are respectively included as redundancy [10, 45].

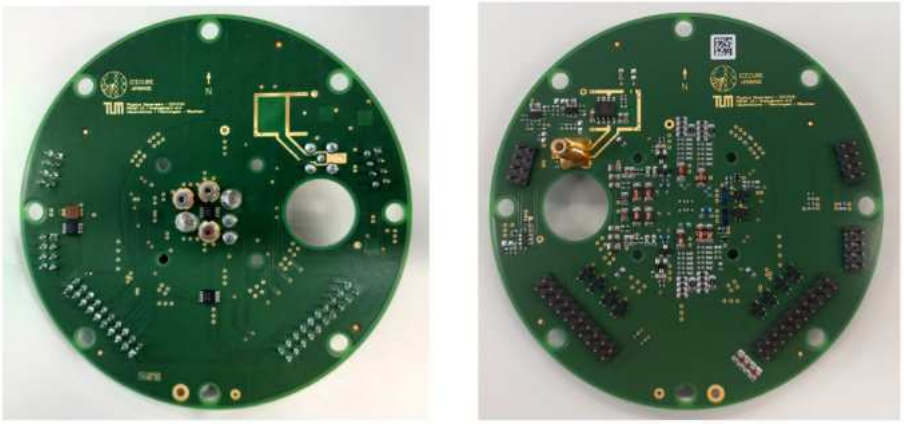

Figure 4.6.: Top (left) and bottom (right) view of the Analog board (AB). It hosts the physical flasher functionality including all six emitters and the corresponding pulse drivers.

Finally, the light that is emitted by the L(E)Ds is guided through a semi-transparent diffusing sphere to make the light pulses as isotropic as possible. The sphere is made of optical teflon where photons are reflected isotropically inside until they eventually are transmitted. Furthermore, the sphere is placed onto a shadow mount whose surface is coated to reduce reflections and precisely control the isotropic light emission [10].

Figure 4.7.: Diffusing sphere mounted onto the shadow mount which hosts the self-monitoring photodiode and SiPM. Glass hemsiphere next to it.

5. POCAM Characterization Procedure

This chapter presents the main work of the thesis: the testing and characterization of the first six Precision Optical Calibration Module (POCAM) devices. It details the characterization procedure, with focus on the temperature-dependent performance of the devices, along with technical challenges, intermediate steps, and the results obtained. The work primarily involved software development, refinement of the characterization setup, and hardware installations of the POCAM devices and other components, ultimately leading to a (semi-)automated characterization procedure.

5.1. POCAM Parameter Set

As the general structure of POCAM and its main components have been discussed in the previous chapters, this part should create the link to what was actually to be tested and characterized throughout the production. Therefore, it is helpful to first have a look at the POCAM parameter set[1], including the corresponding values that may be applied in the context of calibration applications in IceCube.

When a certain POCAM device should be operated, the first selection is about the **hemisphere** that should be emit light. POCAM can be operated simultaneously on both sides, while each hemisphere can also flash independently. One hemisphere of every POCAM device is commonly referred to as “master”, while the other one is called “slave”.

After that, the specific settings for the **emitter** on the selected hemisphere have to be assigned. For the LD-type driven diodes, this includes setting up the correct discharge path that is associated to the selected emitter. For the Kapustinsky-driven diodes the appropriate capacitor bank that should be charged has to be chosen, to flash the correct emitter. Furthermore one of the high-voltage (hv) paths, that effectively control the **emission intensity**, has to be chosen. The paths that can be selected for the LD-type and Kapustinsky driven diodes are commonly called “lmg1” and “lmg2” or “kapu1” and “kapu2”, respectively. This freedom, which is primarily motivated from redundancy, actually enables to address and operate both hemispheres of a single

[1] In the following, the associated names of the mentioned POCAM parameters will be denoted in quotation marks either explicitly in the text or in brackets.

POCAM device independently. This was especially useful to improve the isotropy of the devices by being able to apply independent voltages, as the hemispheres are in principle interchangeable but can never be perfectly equal in their properties. The applied voltages are determined by setting a numerical "PWM" value in the range[2] of 0 - 54000 which linearly correspond[3] to physically applied 0 - 32 V. Accordingly to the names of the hv paths, the emitters that make use of the LD-type drivers are called LMG365, LMG405, LMG450 and LMG520, and the ones that are based on the Kapustinsky drivers are called KAPU405 and KAPU465, with the numbers indicating their nominal emission wavelength.

The selection of the **pulse-widths** is inherently different for LD-type and Kapustinsky driven emitters. The latter one have two physically distinct configurations, as discussed in 4.2, which enable the generation of two pulse widths, one shorter and one broader pulse, that are referred to as "fast" and "default" ("mode"), respectively. The LD-type drivers in contrast allow for a multitude of selectable pulse widths. The phase-shifts of the enable and disable signals, which are responsible for the pulse shape, are determined by the values that are set for the "coarse" and "fine" parameters. The coarse parameter should be set in integers of 0 - 3, while the fine parameter may be chosen from 0 - 47. Varying these parameters by one unit nominally shifts the delay of the disable signal with respect to the enable one by 10 ns and 0.2 ns, respectively. The schematics in 5.1 outlines the phase-shift of an enable (In+) and disable (In−) signal that generates the pulse shape for an LD-type driven emitter. Figure 5.2 shows how the phase-shifts behave by varying the coarse and fine parameters.

Lastly, as POCAM emits single light pulses, the **flashing frequency** can be set to different values. This is done by defining the flashing period ("pulsePer"), i.e. the time between two pulses, in multiples of 17.067 μs. The value for this parameter should be set in multiples of 3, to secure a fixed time delay between trigger signal and light emission. This is necessary, since the generation of the trigger is based on a 60 MHz clock, while the central base clock on the ICM runs on 20 MHz. Furthermore, the value is preferably set to higher values ($\geq$ 30) to guarantee for a consistent intensity over many single measurements and to allow for a full readout of the self-monitoring data.

Throughout the characterization procedure, different settings of the parameters are used to determine its performance. This especially includes a temperature-dependent characterization of the emission intensity, the spectral emission profile and the time profile of emitted light pulses, which has been the main focus of the work presented in this thesis and is discussed in detail in 5.3.1. Additionally, section 5.2 gives an overview on the calibration of the achievable isotropy and number of emitted photons.

[2] Technically the PWM value is documented to be chosen up to 65535, but was limited throughout the development of the procedure to 54000 to protect the components.

[3] 5.3.1 includes a characterization of this correlation.

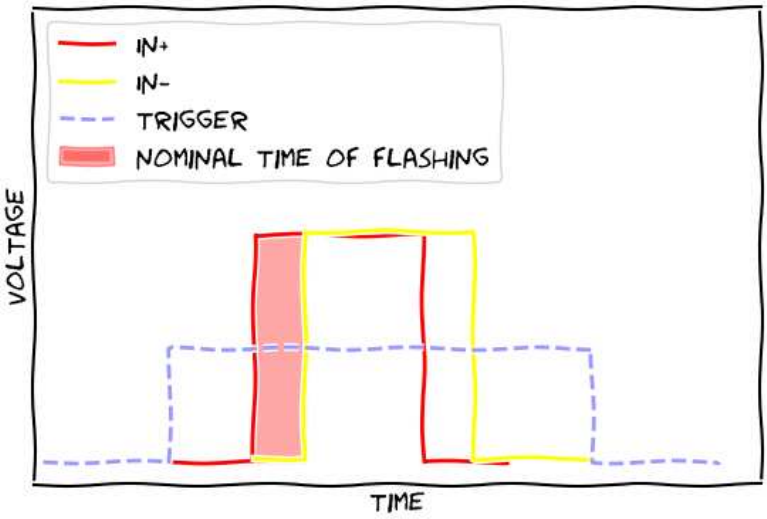

Figure 5.1.: Enable (In+) and disable (In−) signals that are generated upon the trigger signal. The phase-shift of the two determine the nominal time flashing and pulse-shape of the light emission for LD-type driven emitters.

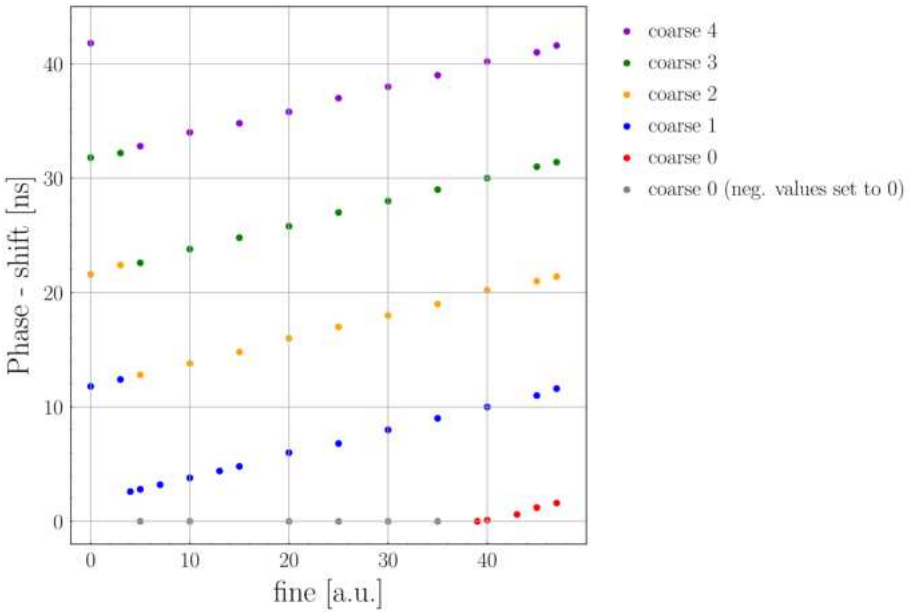

Figure 5.2.: Phase-shifts between the enable and disable signals used to generate the pulses for the LD-type driven emitters. The plot shows the correlation of the phase-shift for several different combinations of coarse and fine parameter. Note that the phase-shift is not the final pulse width as this further depends on the properties of the used transistors, capacitors and inductances, as well as the response of the emitters.

5.2. Calibration of Isotropy and Number of Emitted Photons

An essential property of POCAM, that is characteristic for each hemisphere, is the angular emission profile. It is expected to be rather stable for changes in temperature and variations of POCAM parameters, as it is mainly determined by the properties of the diffusing sphere and the geometric design of the device. Thus it was sufficient to conduct the calibration of the emission profile only at normal conditions and using one single set of parameters. The angular calibration was conducted in a darkbox in which the hemisphere that shall be tested is mounted onto a rotation stage on one side. Figure 5.3 shows a schematic illustration of the complete setup that was used for the angular calibration.

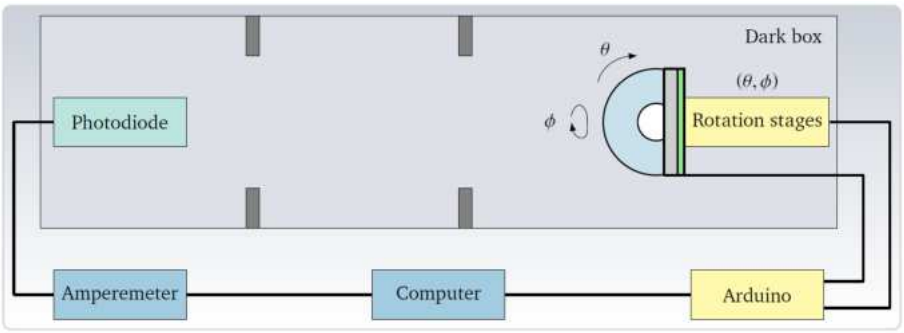

Figure 5.3.: Schematic illustration of the angular calibration setup. On the right side the hemisphere is mounted on the rotation stage. On the left side the photodiode is mounted to detect the light emission. In between, intermediate light baffles are used to reduce stray light and only detect photons that are directly emitted from the hemisphere [10].

The rotation stage turned the hemisphere under two angles, zenith θ and azimuthal ϕ, to scan its angular emission profile. On the other side of the box a NIST-calibrated[4] photodiode was mounted to detect the emitted light. It was connected to a Picoamperemeter that read out the electrical current that has been produced by the photodiode. By scanning the light output of the hemisphere over a finite number of angles, its angular emission profile could be determined. In zenith direction the emission profile was scanned symmetrically over a total range of 150° in increments of 10°. The azimuthal rotations around the POCAM's body axis covered a total angle of 360° in increments of 60°. Figure 5.4 shows an example for the angular emission profile based on the characterization data for the first characterized hemisphere 01.

[4]The photodiode was calibrated by the National Institute of Standards and Technology, which allows to calculate the true number of emitted photons with good precision.

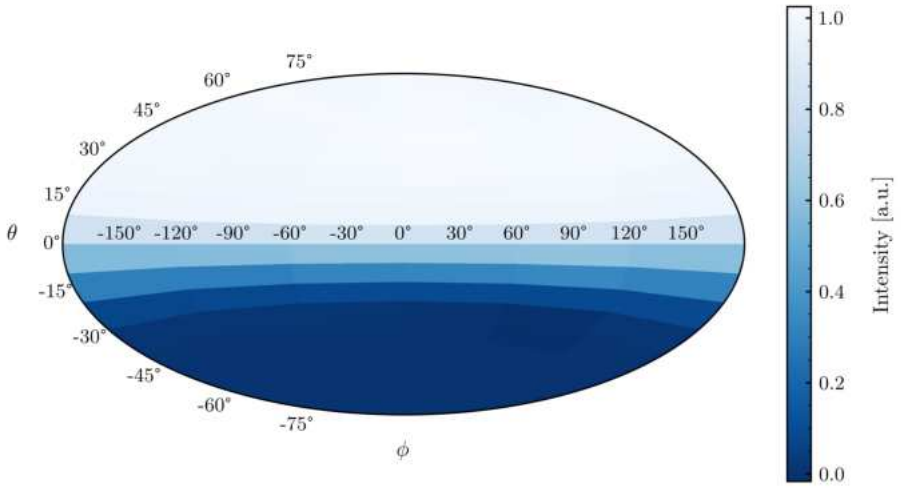

Figure 5.4.: Emission profile of hemisphere 01. The front view when the POCAM hemisphere directly pointed towards the NIST-photodiode is characterized by $\theta = 90°$. The values are normalized to the maximum located at $\theta = 90°$ and $\phi = 0°$. Angles that exceed the scanned range in θ are set to zero.

The emission profile primarily depends on the θ angle, while it is fairly constant for rations under the ϕ - axis. For a complete emission profile, the light emission of the two hemispheres belonging to the same POCAM device had to be combined. Figure 5.5 shows the complete emission profile on the example of the first fully characterized POCAM device. The figure shows the final profile after matching the emission intensities by individually adjusting the applied voltages for the hemispheres. Further, a correction function[5] was applied, that accounted for the different refractive behaviour for transitions from glass to ice compared to using air as outer medium. In ice, photons show a higher probability to be reflected backwards, which reduces the total effective light emission as they may be absorbed and further influences the angular emission profile. The correction function is necessary since the characterization was conducted in air, but the determined emission profiles should display the actual performance in ice. By such, an isotropy of typically $\leq$ 5 - 8 % was achievable.

[5]The correction function is based on the comparison of simulated emission profiles that use air and ice as outer medium, respectively [10].

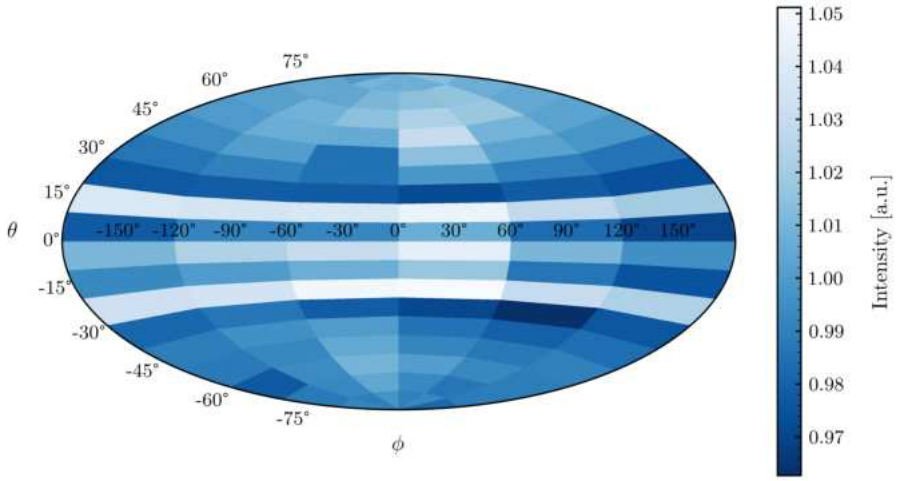

Figure 5.5.: Relative emission profile $f(\theta, \phi)$ of the first produced POCAM device, encompassing hemispheres 01 and 02. The values are normalized to the mean value. Both hemispheres were scanned individually and the data was combined afterwards.

Additionally, the total number of emitted photons could be calculated from the relative emission profile $f(\theta, \phi)$. Apart from the geometry of the setup, this strongly depended on the responsivity $R = \eta \frac{e}{hc/\lambda}$ of the photodiode with its quantum efficiency η. Since the knowledge on the responsivity highly affected to which precision the number of photons could be determined, a NIST-calibrated photodiode had been included to the setup. The total number N_γ of photons emitted over the whole solid angle is given by

$$N_\gamma = \frac{\overline{N_\gamma}}{\Delta\Omega} \int_0^{2\pi} d\phi \int_0^{\pi} d\theta \, \sin\theta \cdot f(\theta, \phi) \tag{5.1}$$

where $\Delta\Omega$ is the solid angle that was covered by the photodiode's active area, as it was seen from the hemisphere. $\overline{N_\gamma}$ is the corresponding mean number of photons that was emitted over $\Delta\Omega$ and has been used as normalization for the relative angular emission profile. It could be calculated by

$$\overline{N_\gamma} = \frac{\bar{I} \cdot T}{R \cdot hc/\lambda} \tag{5.2}$$

Here, T is the flashing period of POCAM and $\bar{I}$ is the mean current that was measured by the Picoamperemeter over all scanned angles θ and ϕ.

The following table 5.1 shows examples of typical values for the total number of photons emitted per pulse, that were achievable with a single POCAM hemisphere. The values were calculated analogously to 5.1-5.2 and were based on the emission profiles of all six emitters using parameter settings that produced intensities that were amongst the brightest achievable by POCAM.

	Number of photons per pulse
LMG365	1.0×10^9
LMG405	1.1×10^{10}
KAPU405	1.2×10^9
LMG450	1.1×10^{10}
KAPU465	1.2×10^9
LMG520	2.1×10^9

Table 5.1.: Typical values for the number of photons that were maximum achievable per pulse with a single POCAM hemisphere. The data is based on the characterization of hemsiphere 02 at 25 °C, PWM= 54000 and coarse= 2, fine= 20 or default mode for LMG or KAPU emitters, respectively.

Beyond the determination of the angular emission profile and the calculation of the number of emitted photons, the setup was also used to calibrate the photodiodes that are installed in POCAM to provide self-monitoring. Therefor, the photodiode was mounted to the setup analogously to the NIST-calibrated one. By comparing the output currents to the one of the NIST-calibrated PD, the photodiodes' responsivity could be determined.

5.3. Temperature-Dependent Characterization

5.3.1. Characterization Setup

Since POCAM will be deployed into ice, the performance had to be characterized for the typical temperatures it will be exposed to. Similar to the angular calibration, each hemisphere was characterized individually. Therefor, an assembled hemisphere stack was mounted into the characterization stage inside an industrial freezer. Figure 5.6 shows an example for a hemisphere stack that was mounted into the characterization stage as it can be seen in 5.7.

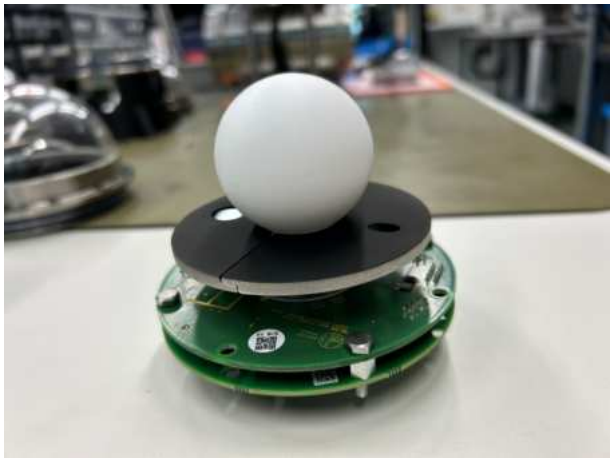

Figure 5.6.: Hemisphere stack to be mounted into the characterization stage inside the freezer. It mainly consists of a diffusing sphere, a shadow mount as well as an analog and digital board.

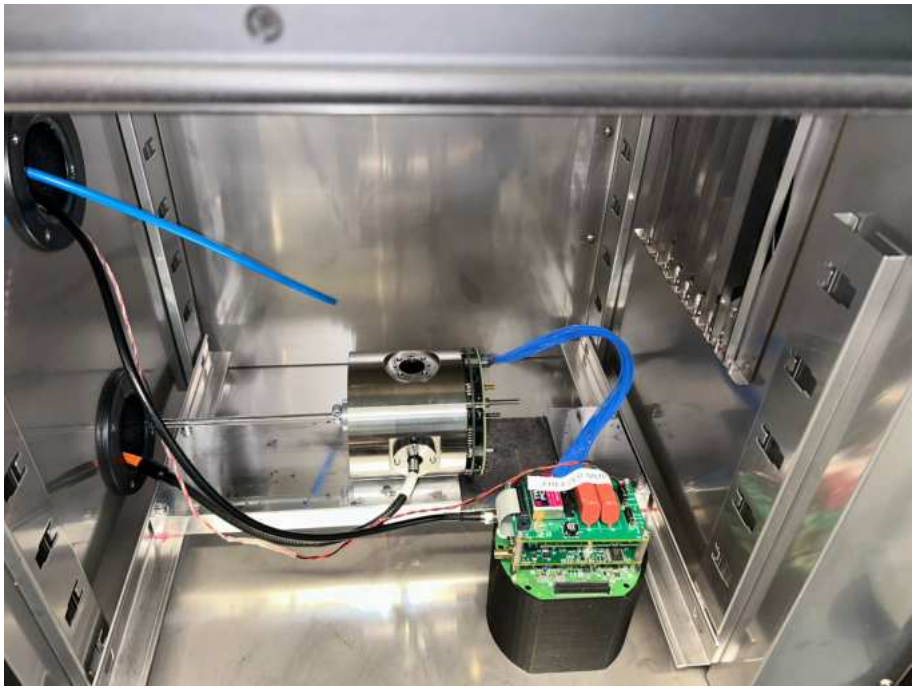

Figure 5.7.: Characterization stage inside the freezer with an exemplary set of the necessary components that had to be installed.

The hemisphere was fixed onto a small cylindrical steel frame in such a way that the shadow mount and diffusing sphere were contained inside. For further stability the frame was attached onto a metal plate. The frame hosts three ports that were used to plug optical connections to it and collect the light that has been emitted by the installed POCAM hemisphere. The digital board of the hemisphere was connected to the designated side of the interface board, which was placed next to the steel frame. Since the characterization procedure required a mini-main board that was slightly adjusted by an additional connector to read out the generated trigger signals, a single MMB was used for the characterization of all hemispheres. The MMB was further electrically connected to a mini-fieldhub (MFH) that was placed outside of the freezer. The MFH has been developed by the IceCube collaboration and was used to provide proper IceCube communication interfaces. The MFH was connected to the same PC as all necessary measurement devices and the freezer, such that the complete characterization procedure could be controlled from the same machine.

Additionally, the freezer was flushed with gaseous nitrogen to reduce humidity inside and avoid water freezing on the boards and other components which could skew the electrical and optical properties of the hemisphere or even damage the boards. This has especially proven useful for the reheating phase after the characterization has finished, as the boards and other components were still cold and warmed up slower than the environment, such that the water in the air tended to freeze on them. It has shown that flushing at a rate of 2 - 3 l/min was sufficient to achieve a relative humidity below 5 % and avoid freezing on the boards.

The several measurement devices used for the characterization were placed inside a darkbox next to the freezer. The region in between, including the apertures to guide the light, were shielded against background by black optical cloth. Optical fibersand a quartz glass rod that were attached to the outlets of the steel frame inside the freezer, collected and guided the light emission to the devices. These included a photodiode (PD) and a photomultiplier tube (PMT), a spectrometer as well as an avalanche photodiode (APD) and a time-to-digital-converter (TDC). The measurement chains that made use of these devices to characterize the different POCAM properties shall be explained in the following.

To characterize the **emission intensity**, two separate measurement chains were incorporated to the setup, of which one used a **PD** and the other a **PMT** to detect the light emission. For both chains the light had been collected and guided to the respective devices by one of the optical fibers. As the setup left space, the light detected by the PD was guided by two optical fibers pointing onto its photoactive area. By this, the light yield onto the photodiode could be increased by around 30 %. The

PD was included first, to detect medium to high light output and covered the largest part of the achievable emission intensities. The setup used a Hamamatsu S2281-01 Si **photodiode**, the same as the ones that are installed in POCAM for self-monitoring. The output current of the PD was fed to a subsequent KEITHLEY 6482 Dual-Channel picoamperemeter that was connected to the PC, which enabled the read-out of the signal. A second photodiode has been added to the setup. It will be used in future procedures to track potential changes of the setup and disentangle actual changes of POCAM. It will be optically connected to an external reference light. The reference light itself will be also optically connected to the steel frame, where the hemisphere will be placed in. During the phases when the hemisphere will not be flashing, the reference light will be turned on and its light will be guided to the first photodiode in the same way the POCAM light emission will be. By comparing the signals of both photodiodes throughout the characterization, potential changes of the setup will be spotted.

The Hamamatsu C13003-01 **Photomultiplier Tube** has been added to the setup in a separate chain to be able to dynamically characterize the light emission even at lower intensities. The output voltage of the PMT, as well as the trigger signal from the mini-main board, were fed to a PC oscilloscope, picoscope6403D from picotech. The trigger signal provided proper timing correlation, such that only signals within a certain time interval were recorded. Due to the high amplification gain and low noise, PMTs typically show a much higher sensitivity compared to PDs. The oscilloscope data was read out via its connection to the PC.

In general, the uncertainty on the determination of the relative light emission could be estimated to 2.6 %, based on earlier efforts during the development of the setup [10]. The measurement uncertainty was mainly driven by picoamperemeter drifts, temperature-dependent fiber couplings and other temperature-induced variations. Likewise, the uncertainty on the absolute light intensity, i.e. the total number of photons, could be estimated to 3.7 % [10].

The characterization of the **time profiles** was the second measurement chain of the setup that made use of the trigger signals from the mini-main board. Here, the light emitted by the hemisphere was guided to an **avalanche-photodiode**, the IDQ id100 single photon detection module, via a quartz glass rod. The APD allowed for the detection of very low levels of light, down to single photons, with high speed and precision. It produced an electric current that was aligned with the arrival time of the photon, which was used as a logical signal for timing purposes. The photo-current of the APD was fed to a **time-to-digital converter**. The setup used a TDC7200 from TEXAS INSTRUMENTS, which had been controlled by an Arduino that was attached to the back of the darkbox. It took the trigger signal from the mini-main board as a

start and the photo-current of the APD as a stop signal. By recording the time lapsed between the both for multiple trigger and photon-hit pairs, the shape of the emitted light pulses that were emitted by the POCAM hemisphere could be reconstructed. In between the glass rod that guided the light pulses and the APD, an optical filter wheel had been placed to control the incident photon flux such that only single photons per pulse were detected. The filter wheel was controlled by another Arduino. Both Arduinos were connected to the PC to control the filter wheel and read out the data for the time profile characterization, respectively.

The uncertainty on determining the time profile with the used setup was primarily driven by the precision of the TDC, that was estimated to 0.2 ns, and the finite number of single timestamps that were taken to reconstruct each of the time profiles [46]. In total, the uncertainty on the reconstructed pulse widths could be estimated to 0.25 ns.

Lastly, the Hamamatsu C12880MA **spectrometer** in the setup was used to determine the **spectral distributions** of the six different emitters. The spectrometer produced an output array of 288 dimensionless numbers, that each scaled with the total amount of incident energy at an associated wavelength. The output array covered a spectral range of 314 - 885 nm in steps of $\sim$ 2 nm. By comparing the output numbers at all wavelength values, the spectral distribution of the incident light could be reconstructed.

Before the characterization of the POCAM devices were conducted, the spectrometer had to be absolutely calibrated. For this, the light of a bright and stable source that will be used as the reference light in future POCAM characterizations, had been guided to the spectrometer. In between six different bandpass and laser line filters of known transmission properties were mounted. Thus, the spectral transmission profile at six different wavelengths that covered the spectral range of POCAM could be reconstructed in an analogous way it was done for the characterization procedure. Comparing this to the true transmission profiles, allowed to determine the correlation between the nominal central wavelength and the one that was measured with the spectrometer, over a broad spectral range. In principle the calibration of the spectrometer was influenced by its spectral response, the variation of the emission intensity of the light source over the spectral range and attenuation effects of the optical fibers. Since the wavelength-dependence of these effects only slowly varied over the spectral range, they could be omitted for narrow pulses, like the ones emitted by POCAM. The result for the conducted spectrometer calibration is shown in figure 5.8. It led to the conclusion that the central emission wavelength could be determined with a precision of around 1.6 nm, which is slightly more conservative than what previous efforts had estimated [10]. For the future it is planned to extend and improve the spectrometer calibration by using a monochromator in combination with the reference light source, such that the spectrometer will be calibrated more precisely and the uncertainty may be decreased.

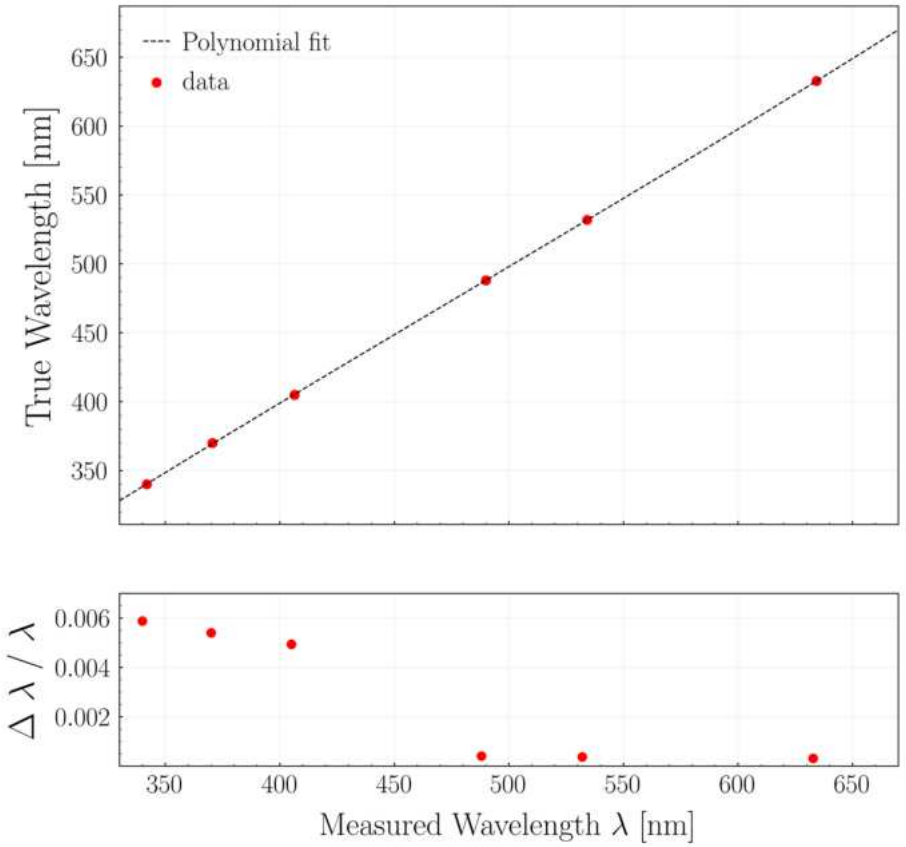

Figure 5.8.: Spectrometer calibration based on using the reference light source and six different bandpass and laser line filters.

The photo below shows the inside of the darkbox containing the discussed measurement devices. Figure 5.10 further gives a schematic overview of the complete setup that was used for the temperature-dependent characterization of POCAM.

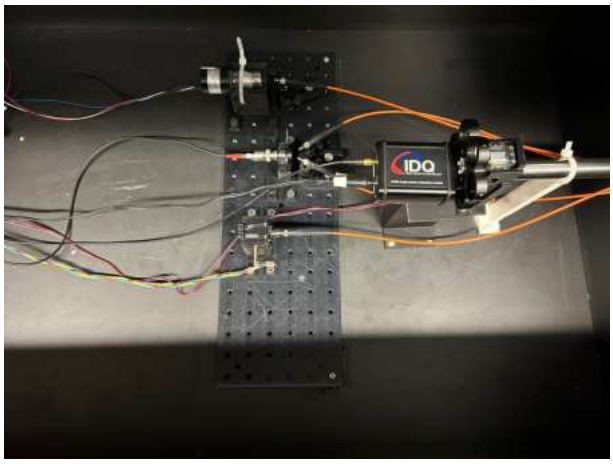

Figure 5.9.: Inside of the darkbox that is used for the temperature-dependent characterization procedure.

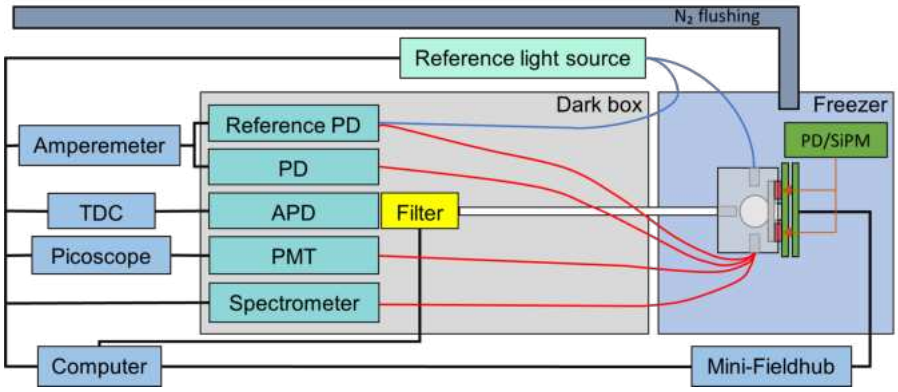

Figure 5.10.: Schemtic illustration of the complete setup used for the temperature-dependent characterization procedure.

5.3.2. Automated Characterization Procedure

Apart from the manual assembly[6] of the hemisphere, its installation into the freezer and preparing the setup, which included providing the nitrogen that had to be flushed to the freezer, the characterization has been conducted in an automated procedure.

The necessary software to communicate to the POCAM device, as well as the main characterization sequence and all other programming routines that were used to control the freezer, the filter wheel and measurement devices, are located on the same computer that is shown in 5.11. The server can be accessed via ssh from any PC that is connected to the same network.

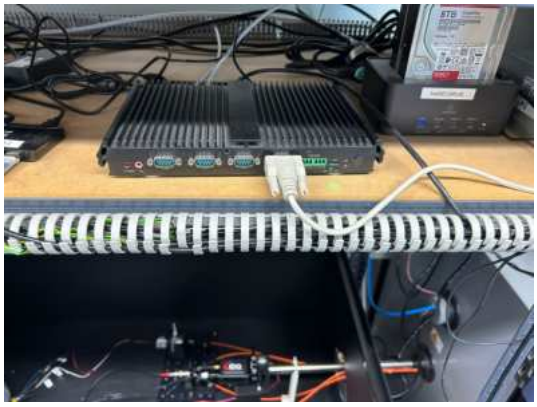

Figure 5.11.: The PC placed on the shelf above the darkbox and next to the freezer, from which the characterization procedure is conducted.

Before the characterization was started by running the main characterization sequence, a short test run has been performed to ensure the basic functionality of the installed POCAM hemisphere and all measurement devices. For this, a test setting of POCAM parameters was used to flash it at room temperature and check the measurement output. During the characterization of the first six POCAM devices, some of the common problems included the filter wheel being not operational or the spectrometer control losing connection.

If the setup has passed the test run, all parameters that should be scanned throughout the characterization had to be set up inside a designated JSON file. This included the temperatures at which the characterization data should be taken. The temperatures that were selected for the first batch of POCAMs were: 25, 0, -10 , -20, -30 and -40 °C. The selection was based on the typical temperatures the devices will be exposed to after

[6] A detailed description for all necessary steps to fully assemble a POCAM device, including the hemisphere stack is given in [47].

deployment. Figure 5.12 shows the ambient temperature in IceCube in dependence of ice depth. As the 21 POCAM devices will be deployed in depths ranging from around 1400 - 2600 m, four temperature values ranging from -40 °C to -10 °C were chosen. The characterization was further conducted at 0 °C. This temperature had been added, since it is planned to already conduct a first IceCube calibration run with POCAM during the deployment, for which the ice is molten to temperatures that are close to the freezing point. Furthermore, it was an intermediate step to the baseline temperature at 25 °. The characterization at the baseline temperature was included to correctly interpret the measured values for light emission that were taken throughout the temperature-dependent characterization to a true number of emitted photons.

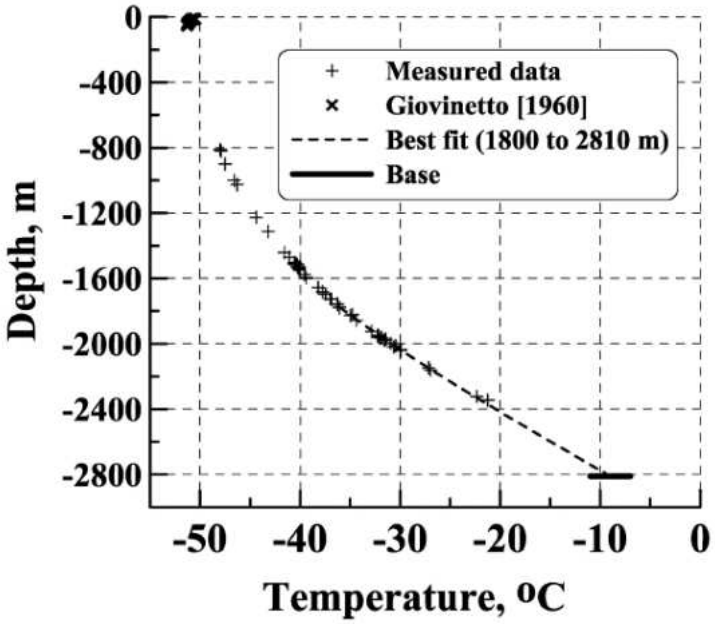

Figure 5.12.: depth vs temperature of the Antarctic ice as used for IceCube [48].

Apart from the temperatures, the JSON file contained the POCAM parameter settings, which the characterization of the hemisphere should be based on. The following table summarizes the several parameters and the explicit values that were set to characterize the first six POCAM devices.

Temp. °C	[25, 0, −10, −20, −30, −40]
Emitter	[LMG365, LMG405, Kapu405, LMG450, Kapu465, LMG520]
PWM	[10000, 14000, 24000, 34000, 40000, 44000, 50000, 54000]
LMG coarse−fine	[0−47, 1−5, 1−20, 2−20]
KAPU mode	[default, fast]

Table 5.2.: Temperature and POCAM parameter settings that were used for the characterization of the first six devices.

The JSON file was handed to the main sequence, which executed the characterization procedure by providing a logical order of the necessary steps and functions. A complete temperature-dependent characterization for one hemisphere took around 40 hours. At each temperature, the hemisphere has been characterized for the selected parameter settings and the data was stored into a designated hdf5 file. Throughout the procedure, the main information of every step that has been executed was printed to the command shell and stored to a logging file, which enabled the user to follow the procedure in real time. Furthermore, throughout the characterization, plots visualized the data such that the basic performance of the hemisphere could already be checked during the procedure.

The subsequent sections give a more detailed discussion of the data acquisition, data processing, examples of results and distinctive features that occurred during the characterization for the first six POCAM devices.

5.3.3. Emission Intensities

As already mentioned, the emission intensity has been characterized by using a PD and a PMT in two separate measurement chains. For the case of the PD, the subsequent picoamperemeter took 100 single measurements. Each measurement resulted in an averaged output current that had been produced by the PD over a measurement interval of 1 power line cycle, which corresponds to 0.02 s. This measurement was conducted twice for every single setting that should be characterized, once while the hemisphere was emitting light and once only measuring background. After subtracting the background, the mean of the 100 pure signal current values was used as a measure for the emission intensity of the hemisphere. Figure 5.13 displays an example for a dataset of 100 measured current values after subtracting the background.

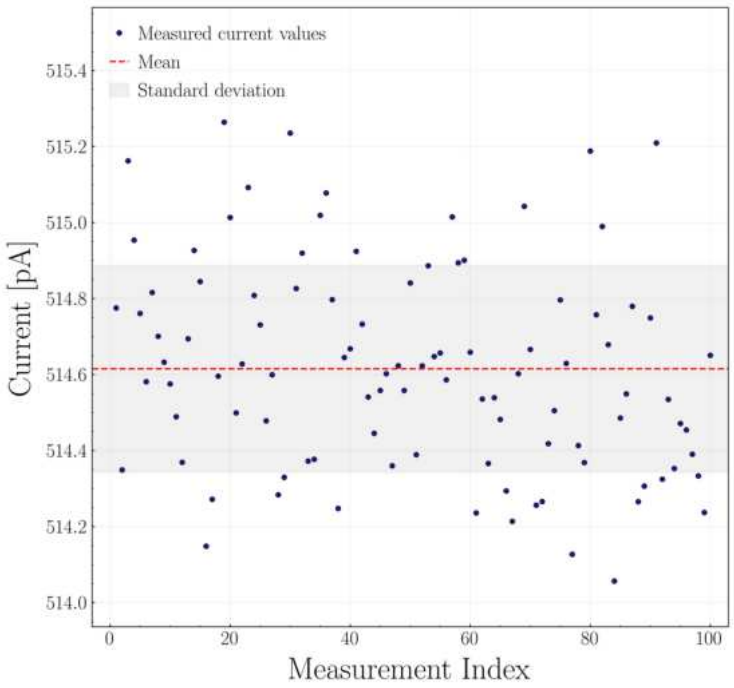

Figure 5.13.: Measured current values to determine the emission intensity by using the PD. The data is based on detecting the light emission of the LMG405 emitter of hemisphere 23 for PWM= 54000, pulsePer= 3, coarse= 2 and fine= 20. The plot shows the measured current values after subtracting the mean background of 0.1 pA.

Normalizing the values to the current that had been measured for the baseline at 25 °C, provided a measure for the relative emission intensity. Since the true emission intensity at the baseline could be determined from the calibration measurements discussed in 5.2, the relative emission intensity could be directly translated to the total number of emitted photons. Figure 5.14 shows a typical result for the temperature-dependent behaviour of the relative emission intensities.

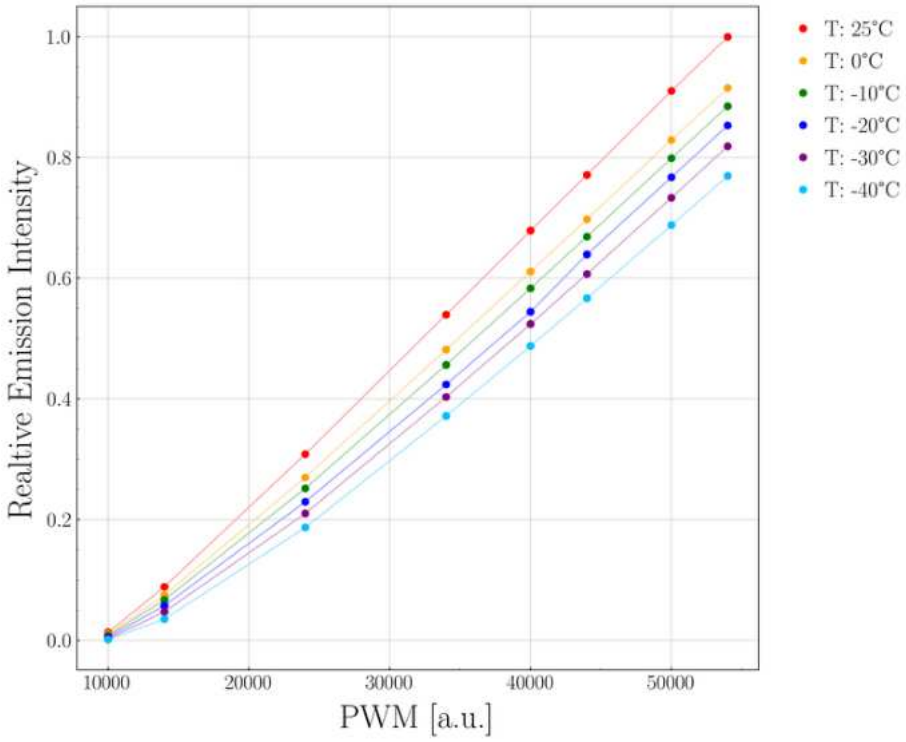

Figure 5.14.: Relative emission intensity as a function of the PWM parameter for different temperatures. The data is based on the data taken with the PD for the LMG405 emitter on hemisphere 23 at coarse= 2 and fine= 20. The data is normalized to the baseline measurement at 25 °C, PWM= 54000, pulsePer= 3, coarse= 2 and fine= 20 for the same emitter. The width of the lines that connect the data points give the standard deviation.

Besides temperature induced changes or varying the applied voltage, the emission intensity was affected by the specific values that were set for the remaining parameters. Under same conditions and using the same PWM value, but changing the pulse width settings, the emission intensity changed as well. Typically, for shorter pulses the intensity decreased, as the time interval in which the discharge current induced light emission in the diodes has been reduced. Figures 5.15 and 5.16 show results for the relative emission intensity for a LMG and KAPU emitter that were operated at different pulse width settings, but same remaining parameters, respectively.

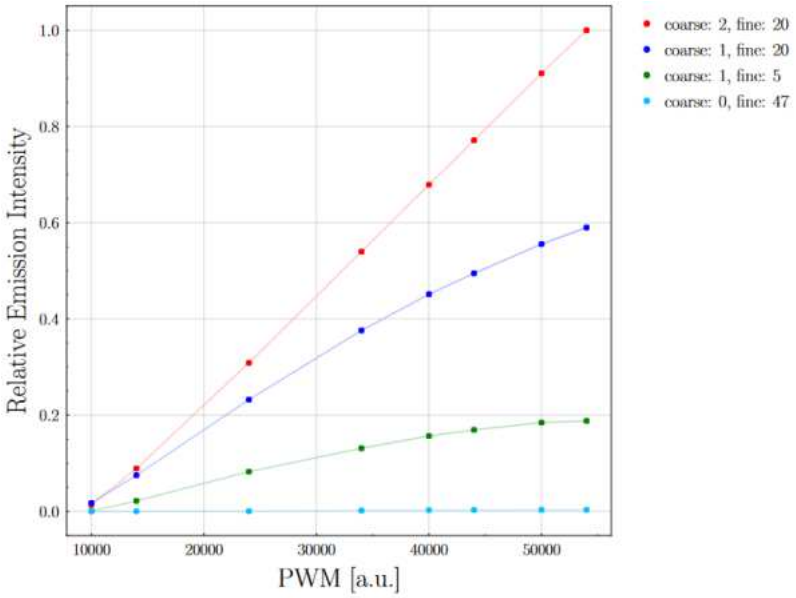

Figure 5.15.: Relative emission intensity for different pulse shape settings at constant 25 °C, PWM= 54000 and pulsePer= 3 for the LMG405 emitter of hemisphere 23. The data is normalized to its brightest light output at coarse= 2, fine= 20.

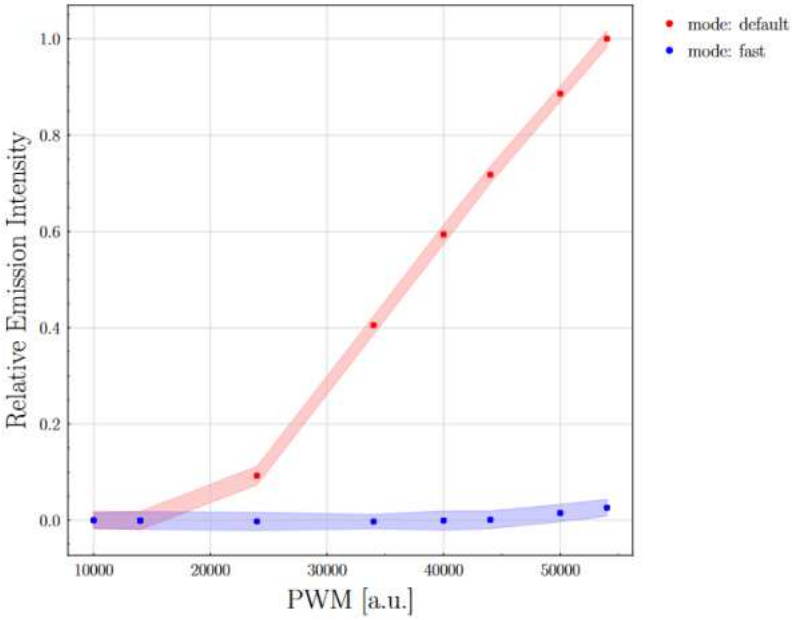

Figure 5.16.: Relative emission intensity for two available pulse shape settings at constant 25 °C, PWM= 54000 and pulsePer= 3 for the KAPU465 emitter of hemisphere 23. The data is normalized to its brightest light output at default mode.

As POCAM operations are based on setting the PWM value, the light emission properties, like the intensities shown above, are commonly characterized in dependence on this quantity. To have a more complete characterization on the behaviour of POCAM, the actually applied voltages were read out as well throughout the procedure. A typical correlation of the two is shown in figure 5.17 below.

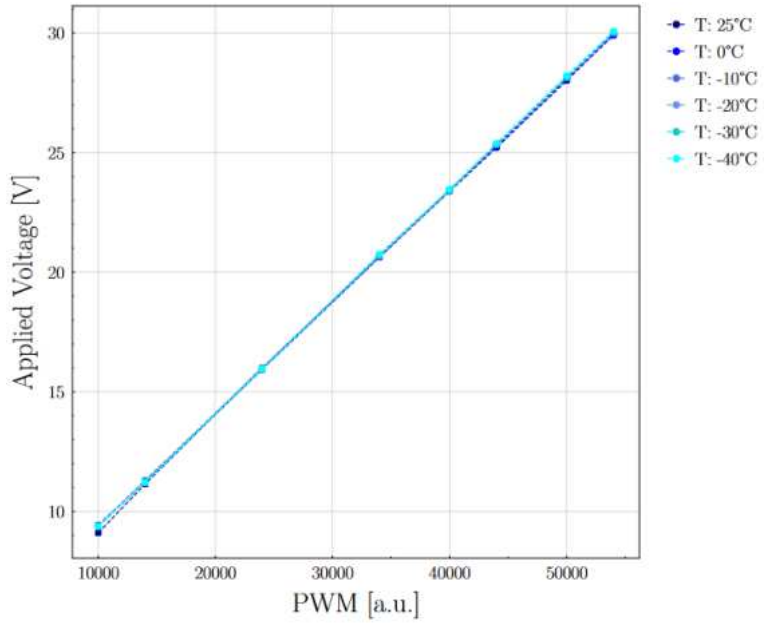

Figure 5.17.: Physically applied voltage vs PWM value at different temperatures for the KAPU465 emitter on hemisphere 16.

The PMT has been added to dynamically characterize the whole range of emission intensities that are achievable with POCAM. Since the PMT was intended to detect fainter light pulses, the measurement was only conducted if the current that had been measured with the PD fell below a certain threshold. So far, this threshold signal was set to 30 pA. The exact value is arbitrary, but should lie well below the saturation limit of the PMT while it should be high enough to still detect a reasonable amount of light. Figure 5.18 shows an example for the output data of the PMT that was read out with the subsequent oscilloscope. Integrating the shape of the produced voltage signal over time, provided a measure for the emission intensity.

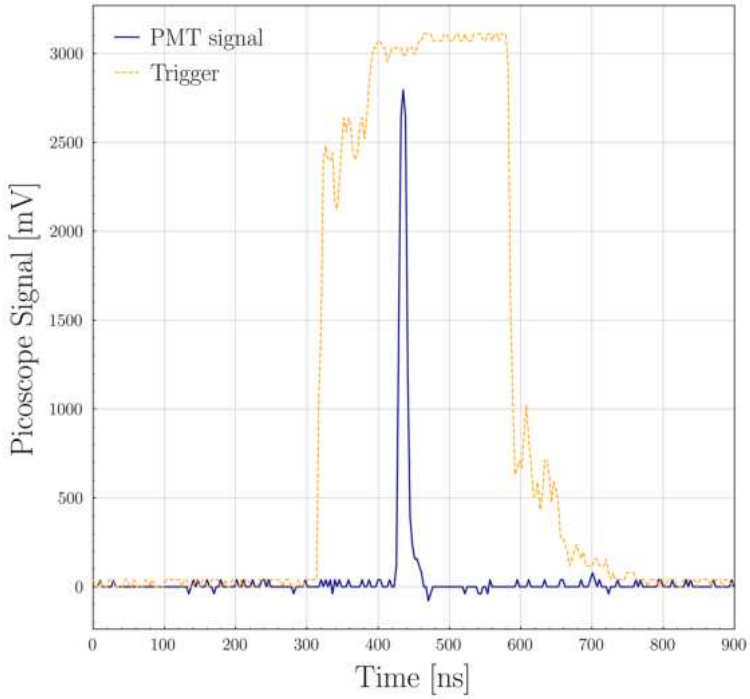

Figure 5.18.: POCAM trigger and PMT data signal, that were fed to the oscilloscope. The PMT data shows the signal detected for the LMG405 emiter on hemisphere 16, operated at 25 °C, PWM= 54000, pulsePer= 3, coarse= 0 and fine= 47.

To translate this again to a true number of emitted photons, the output data had to be compared to the corresponding baseline measurement, analogously to the PD data. However, in the case of the PMT measurements this could only be done for fainter emitters, like usually the LMG365, where the PD output always fell below the set threshold and PMT data was taken for all used settings, including the baseline. For brighter emitters, this was not the case and the PMT data had only been taken for a certain amount of settings. As the PD data has been taken for every set of used parameters, the PMT output data could be cross-calibrated by comparing it to the PD data below the set threshold. Figure 5.19 shows an example for the relative emission intensity as it was taken with the PMT. Figure 5.20 further contrasts the results for determining the relative light intensity by using the PMT and the PD, respectively.

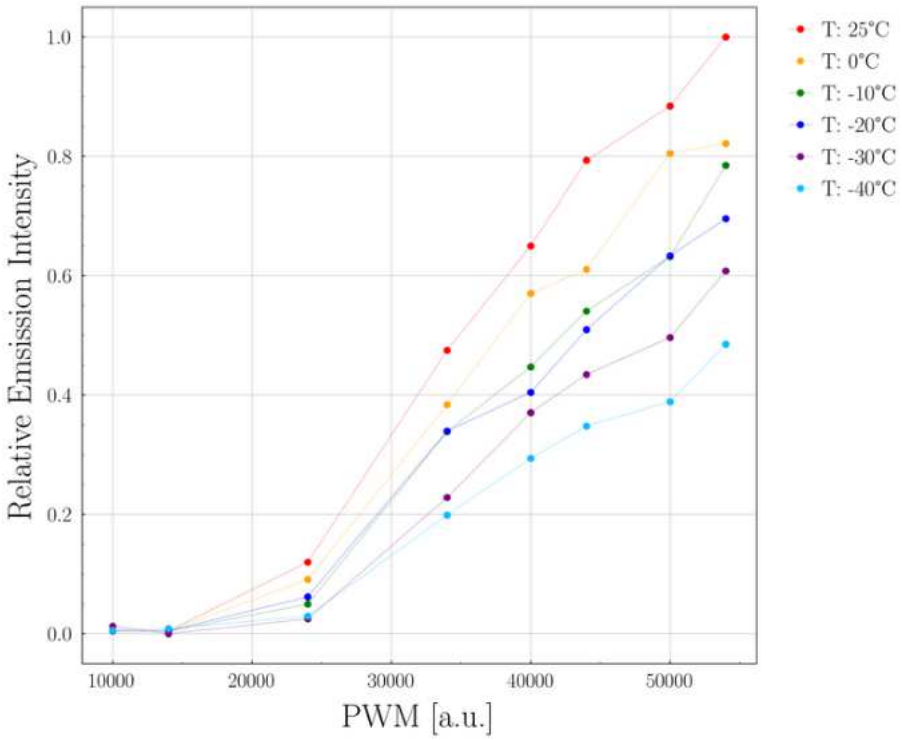

Figure 5.19.: Relative emission intensity for different temperatures as it is measured by using the PMT. The data shows the light emission of the KAPU405 emitter on hemisphere 23 for PWM= 54000, pulsePer= 3 and default mode. It is normalized to the baseline measurement at 25 °C for the same emitter and parameter settings. The width of the lines that connect the data points give the standard deviation.

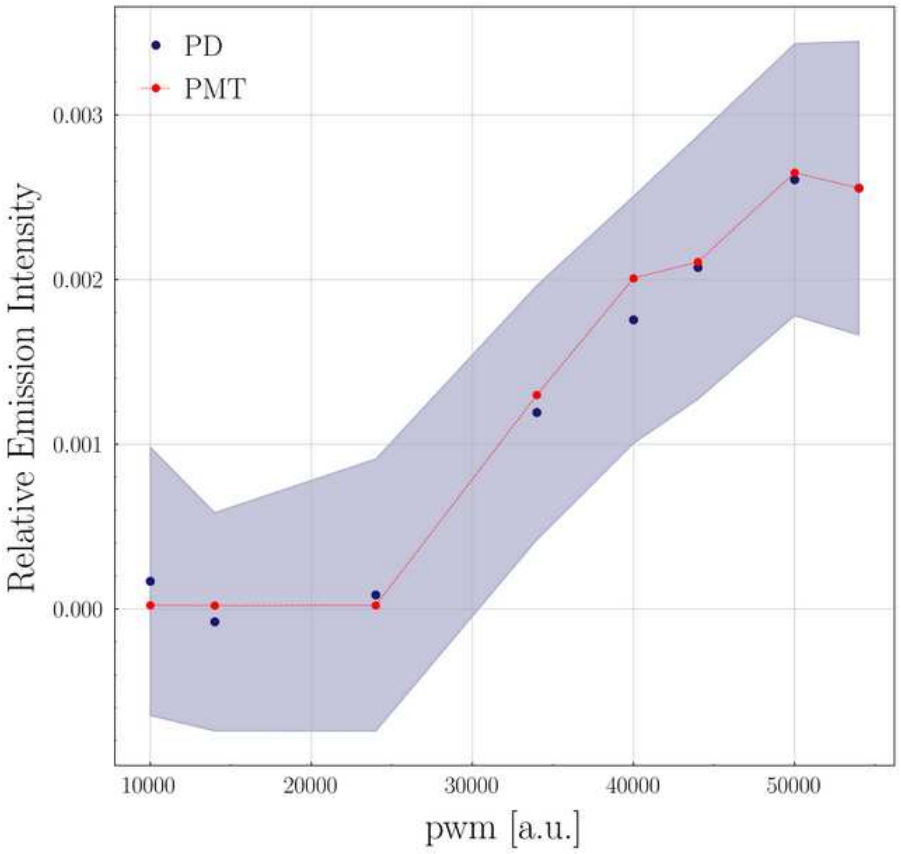

Figure 5.20.: Cross-calibration of the relative emission intensity by using the PMT and PD output signals. The data is based on the light emission of the LMG405 emitter on hemisphere 23 at 0 °C for PWM= 54000, pulsePer= 3, coarse= 0 and fine= 47. The data is normailzed to the baseline measurement of the same emitter at 25 °C for PWM= 54000, coarse= 2 and fine= 20.

The self-monitoring of the emission intensity has not been part of the characterization for the first six devices. The read-out of the onboard PD and SiPM is currently under implementation and will be included for future characterizations. The used PDs, SiPMs as well as the read-out is expected to behave very similar for all devices, such that future characterizations of the self-monitoring sensors may be used to calibrate the self-monitoring of the first six devices as well. Apart from the relative, temperature-induced behaviour of the sensors, this includes an absolute calibration. For this, the self-monitoring sensors will be read out on the hemispheres during the calibration procedure that is done to determine the total number of emitted photons as discussed in 5.2. The self-monitoring can then be calibrated by comparing the data output to the true emission intensity of POCAM.

Another important thing that has to be noted is that throughout the characterization procedure it appeared that the LMG520 emitters are quite prone to fail at lower temperatures. If the emitters had failed, it usually happened at temperatures around -20 °C to -40 °C and did not recover, such that no light emission was detectable anymore. In total 7 out of 24 tested hemispheres showed this problem. The hemispheres with failing emitters were not used for the final production and were left for further investigation which will probably include the replacement of malfunctional diodes. Besides other important features and problems, this is documented in the designated spreadsheets and text files that are deposited for the POCAM production.

5.3.4. Spectral Distributions

The spectrometer measurement was conducted to determine the true emission wavelength of the several emitters. The spectral profile is expected to be rather stable under the variation of POCAM parameter settings. Thus this measurement was conducted more sparsely for only a few settings at every scanned temperature. At every parameter setting the measurement was actually performed for, it was conducted twice, once when the device was emitting light and once only detecting background. To provide best achievable data statistics, the exposure time of the spectrometer was set to the highest possible value, while still remaining below the saturation limit of the spectrometer. The signal and background measurements were then conducted with the the same exposure time. After the background is subtracted, the signal data could be interpreted as a discrete spectral distribution profile of the detected light. The emitted light of POCAM is typically of Gaussian shape. The main information from this measurement were the central-wavelength (CWL) and the full width at half maximum (FWHM), which were obtained by fitting the distributions and deducing the best-fit parameters.

It should be noted that the true CWL of each emitter can differ up to 10 nm from the nominal emission wavelength, depending on the manufacturer's tolerance. Figure 5.21 shows an example for the spectral profile of an emitter as it was measured by the spectrometer.

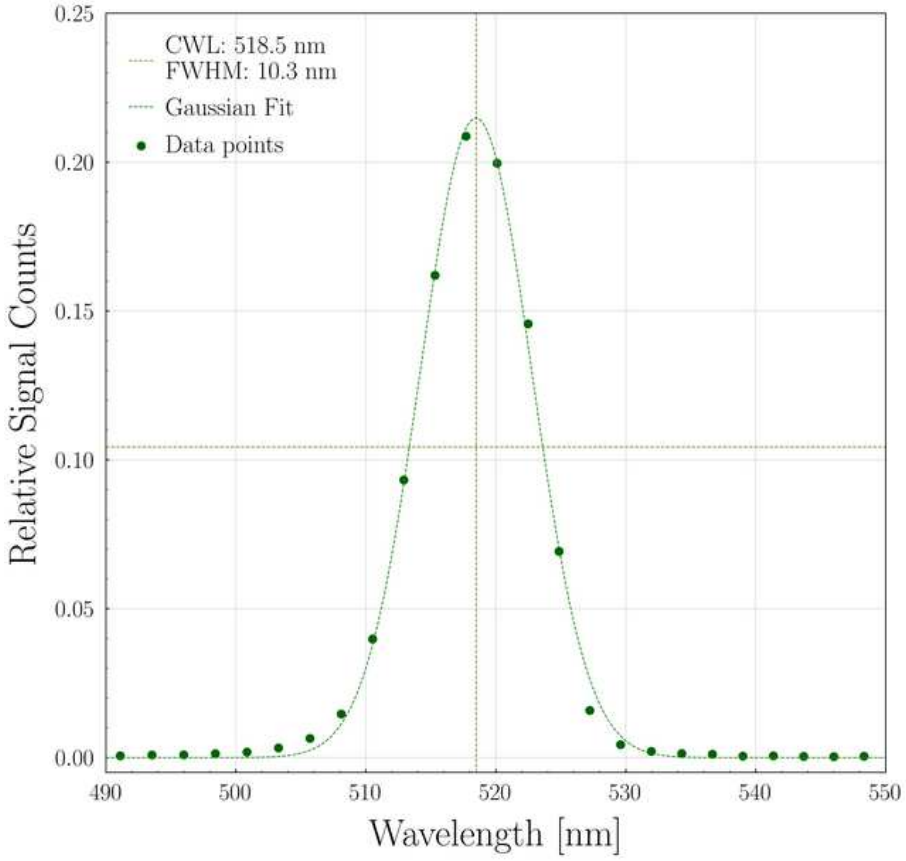

Figure 5.21.: Spectral Distribution of the LMG520 emitter hemisphere 23. The data shows the light emission taken at the baseline at 25 °C, PWM= 54000, pulsePer= 3, coarse= 2 and fine= 20.

The main influence for variations in the spectral profiles was the change in temperature which typically caused a shift towards lower wavelengths for the emitted spectrum, while the width usually stayed stable. Figure 5.22 shows an example for the characterization of the spectral profile for an emitter at different temperatures.

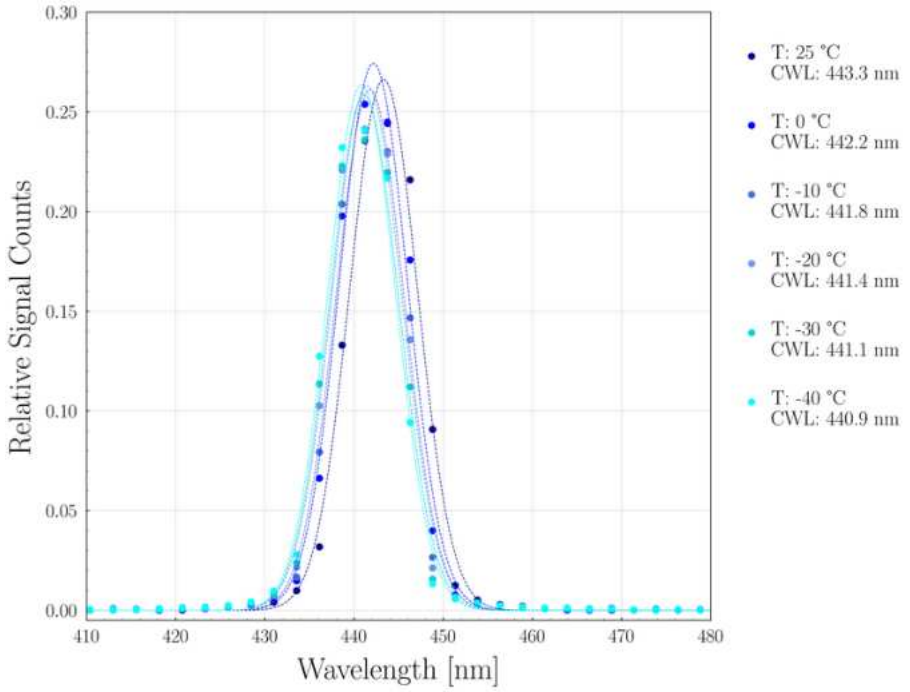

Figure 5.22.: Spectral Distribution at different temperatures for the LMG450 emitter hemisphere 23. The data is based on the light emission for PWM= 54000, coarse= 2 and fine= 20.

5.3.5. Time Profiles

As described, the time profile of the emitted pulses was determined by detecting the light with an APD and measuring the time elapsed between the initialization of the pulse and the arrival time of one single photon of this pulse. The trigger signal which initializes the POCAM emission was diverted from the mini-main board and guided to the TDC, where it acted as a start signal. The output signal of the APD when it detected a photon then provided a corresponding stop signal at the TDC. By measuring the delay between start and stop signal for many trigger signals and photon hits at the APD, the time profile of the emitted pulses could be reconstructed. To conduct the reconstruction with good precision, an occupancy of ≤ 0.1 was targeted. This means that maximum 10 % of the received trigger signals, the APD produced an output signal due to a photon hit. As every single measurement only could produce the timestamp for the arrival time of one single photon of an emitted pulse, it was necessary to attenuate the light emission down to the level where at maximum one photon per pulse hit the APD and created a signal. Photons of the same pulse that arrived later than the first detected one would have been lost, what would have led to a bias towards earlier arriving photons and the true time profile could have not been reconstructed. As the reconstruction of the time profile effectively reduced to a counting experiment, under the assumption a pulse was actually detected, an occupancy of 0.1 resulted in a probability for only a single photon to arrive at the APD of

$$\frac{P(k=1)}{P(k\geq 1)} = 95.08\ \% \tag{5.3}$$

which means that in less than 5 % more than one photon has arrived at the APD, under the condition the emitted pulse was detected at all and a timestamp was generated. However an occupancy of ≤ 0.1 means that ≥ 90 % of the pulses were not detected at all and as such provided no information. Due to time consumption, the lower threshold for the occupancy for which a full time profile measurement has been conducted was set to 0.005. To achieve suitable occupancy values, the emitted light was guided by a quartz glass rod. The glass rod had been included in this measurement, as the initially used optical fiber could not collect enough light to reconstruct the time profiles for many pulse-width settings. The glass rod, which significantly increased the light collection, together with the filter wheel, that was placed in between the glass rod and the APD, allowed to achieve suitable occupancy values. The filter wheel hosted six apertures to mount filters which lowered the occupancy. The first position of it was left empty while the remaining five are equipped with neutral density filters of increasing attenuation. If the occupancy exceeded the threshold of 0.1, the wheel turned to the next filter. Once the occupancy matched a value between 0.005 and 0.1, a complete

measurement was performed. After the TDC had measured 9000 timestamps, the data was stored and the pulse width could be deduced. For the Kapustinsky-driven emitters both modes, default and fast, were tested, whereas for the LMG emitters out of all possible coarse and fine settings, four distinct combinations that produce relevant pulse-widths were selected for the characterization. The selected settings 0-47, 1-5, 1-20 and 2-20 typically covered a pulse-width range from 2.5 - 15 ns.

Examples for time profiles that resulted from the different pulse-width settings as used for the LMG and Kapu emitters throughout the characterization procedure are shown in the figures 5.23 and 5.24, respectively.

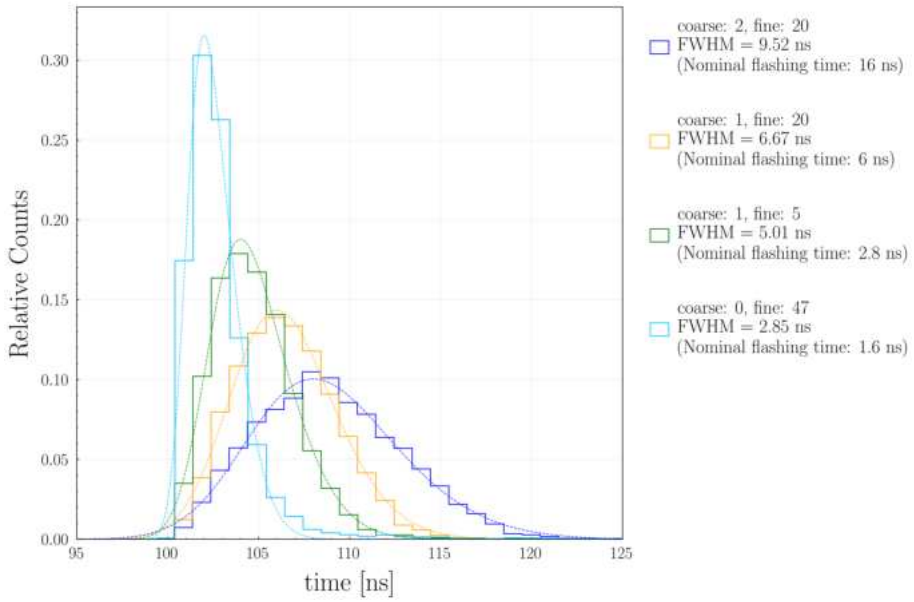

Figure 5.23.: Time profiles of emitted light pulses for the LMG405 emitter on hemisphere 23. The data is based on the light emission at -20 °C, PWM= 54000, pulsePer= 3 and the four different coarse and fine combinations as used throughout the characterization procedure.

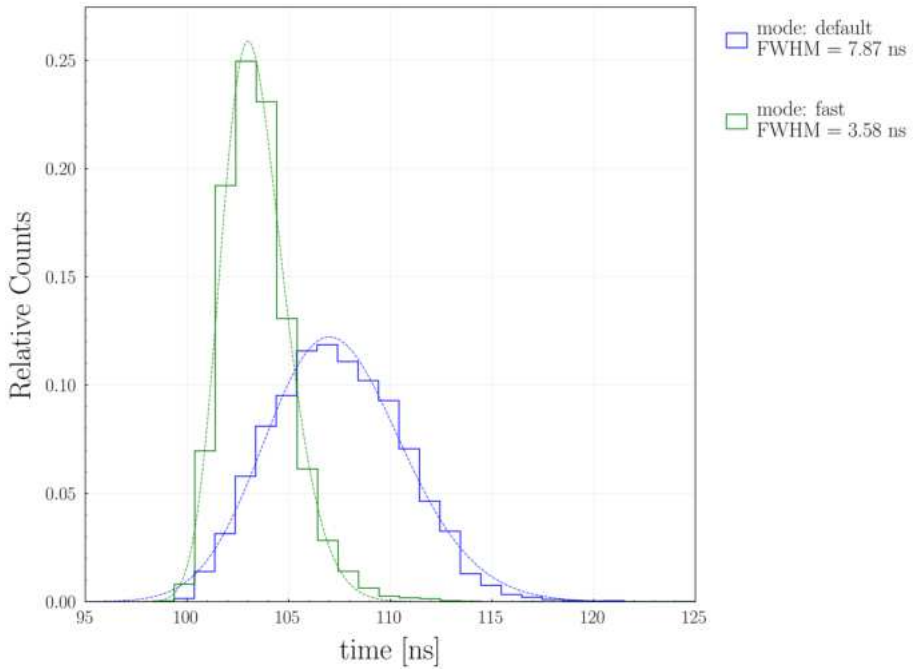

Figure 5.24.: Time profiles of emitted pulses for the KAPU405 emitter on hemisphere 23. The data is based on the light emission at -10 °C, PWM= 54000, pulsePer= 3 and the two available pulse shape modes.

The shape of each time profile could typically be fitted by a (skew) normal distribution, from which the deduced FWHM had been the main information to determine the pulse-width. For most of the emitters and used parameter settings, the time profiles stayed relatively stable under varying the temperature. The pulse widths usually deviated by less than 1 ns over the scanned temperature range.

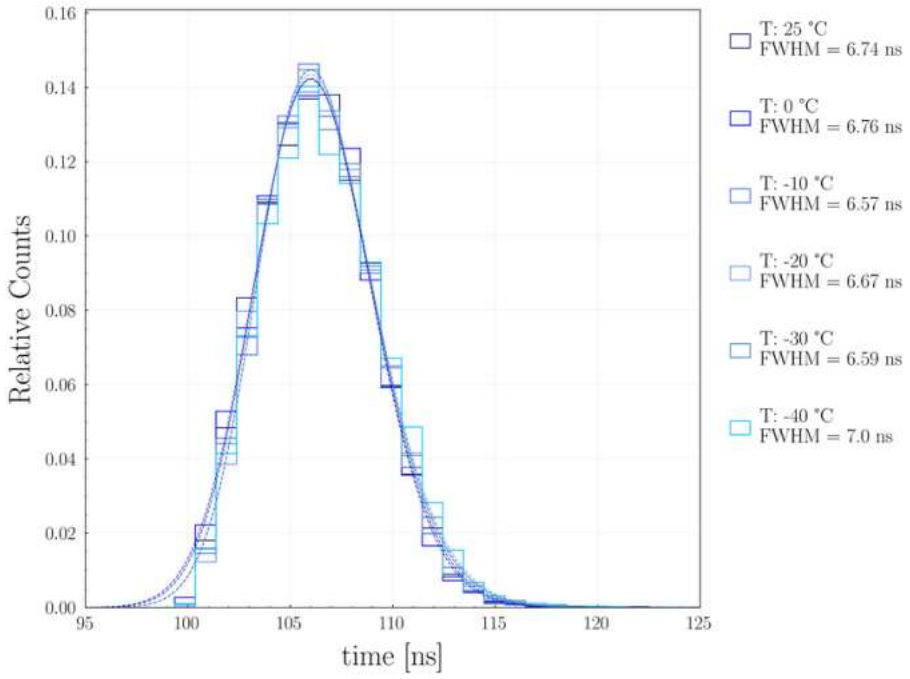

Figure 5.25.: Pulse shape at different temperatures for the light emission for the LMG405 emitter on hemisphere 23. The data was taken for PWM= 54000, pulsePer= 3, coarse= 1 and fine= 20.

The exact behavior of the pulse shapes could not be generalized and strongly depended on the specific emitter of the hemisphere that was characterized. However, for the lowest temperature at -40 °C, the pulse width typically took the largest value.

Furthermore, at lower temperatures the pulse shape that was produced by setting coarse= 0 and fine= 47 for LMG emitters, tended to heavily broaden. The exact reason for that is still unclear. One idea was to investigate the delay of the enable and disable signals that are used to generate the pulse shapes and see if it is prone to clock jumps or misalignments. However, this could be excluded. An explanation that the signal would be strongly influenced by background would have been in agreement with the generally very faint light emission for this pulse-width setting, which typically further decreases at lower temperatures. But due to the specific shape that only showed a long right-sided tail, this could neither be the reason. It appears that the tail is a generic feature, but was suppressed by the high intensities within the short main interval of the pulse. For very faint light emissions the tail seemed to contribute significantly to the total time profile.

The following figure 5.26 shows a typical result of the pulse broadening for coarse= 0 and fine= 47 at −40 °C, compared to its regular shapes at higher temperatures.

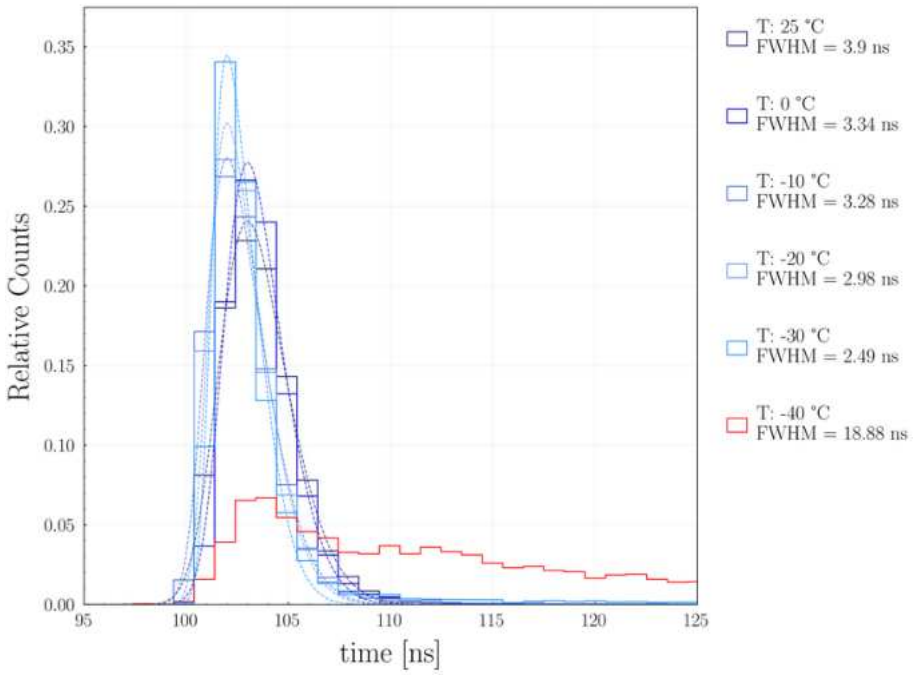

Figure 5.26.: Pulse broadening for the light pulses that are emitted for coarse= 0 and fine= 47. The data is taken for the LMG405 emitter on hemisphere 16 at PWM= 54000 and pulsePer= 30.

Apart from the pulse broadening for this specific pulse-width setting, the LMG520 emitter on every hemisphere showed distinct pulse shapes for their light emission compared to the other emitters, irrespective of the exact pulse settings that were used. In general the emitted pulses were significantly broader and showed longer tails. For low enough emission intensities the broad pulse shape was typically resolved into a main peak which was closely followed by a second one. As this appeared to be a special feature of the used LMG520 emitters and did not occur for other emitters, it could be excluded that it has been caused by clock jumps or similar and was most likely due to distinct properties of the installed diode. The following figure 5.27 shows the generally broadened pulse shape for LMG520 emitters, as well as the resolved double peak.

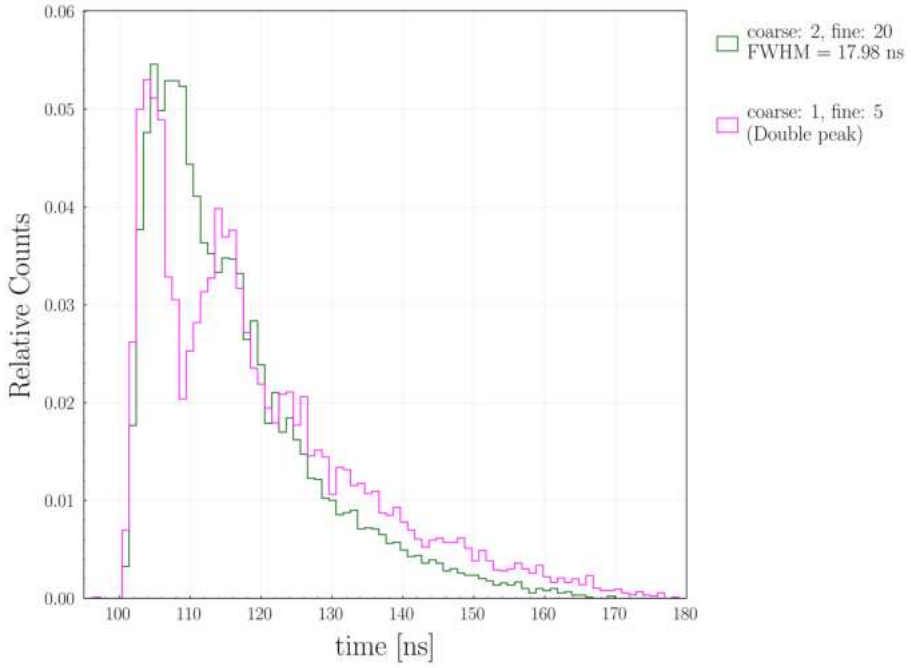

Figure 5.27.: Example for the generally broad pulse shape for the light emission of all LMG520 emitters, which is resolved into a double peak for pulse width settings for nominal narrow pulses. The data is taken for the LMG520 emitter on hemisphere 23 at -40 °C PWM= 54000 and pulsePer= 3.

Likewise as the pulse-width settings influenced the emission intensities, the applied voltage vice versa showed an impact on the final pulse shape. In general lower voltages, i.e. smaller PWM values, resulted in shorter pulses, as there was less total charge that had to flow through the diodes and initialized the light emission. An example for the result for this is shown in figure 5.28 below.

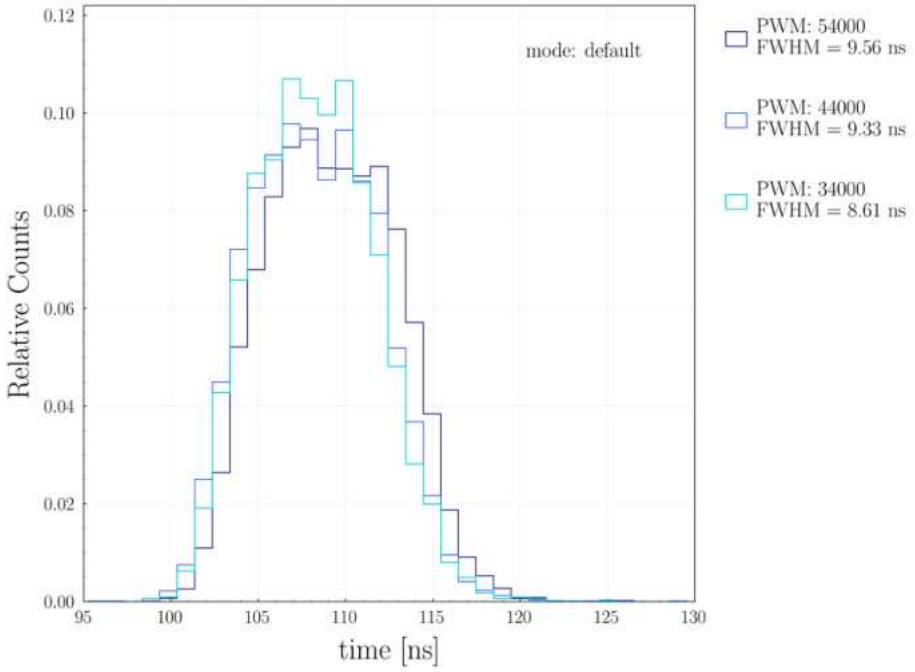

Figure 5.28.: Influence on the pulse shape of changing the PWM value for constant pulse-width setting. The data was taken for the KAPU465 emitter on hemisphere 23 at -20 °C, PWM54000, pulsePer= 3 and default mode.

Finally, it should be noted that the time profiles, shown in the figures 5.23 - 5.28, were virtually shifted if required, such that the pulses showed the same starting point in time. The respective time shifts of the pulse profiles arose from the different clock cycles on the ICM, such that the pulses were initialized at different delay times after receiving the trigger signal. The different internal delays between trigger signal and start of the light emission resulted in horizontal shifts of the time profiles. For final calibration applications in IceCube, the start of the light emission can be tracked precisely by the self-monitoring sensors of POCAM, such that these shifts in time due to internal delays will not matter. Hence, it was sufficient to characterize the time profiles relative to an arbitrary starting time.

5.4. Summary and Future Outlook of Final Acceptance Testing

In total, 24 hemispheres were tested for the production and characterization of the first batch of POCAM devices. 10 of these hemispheres did not pass the characterization tests, due to the following reasons:

- 7 hemispheres were removed because the LMG520 emitters failed during the temperature-dependent characterization
- 2 hemispheres had scratches on the diffusing sphere and shadow mount and were removed
- 1 hemisphere showed very low light emission from its LMG405 emitter as well as a very broad tail in the time profiles of its incorporated LMG450 emitter and was therefore not used for production

During the characterization of hemisphere 09 it was noticed that the diffusing sphere had a small groove on its surface, however further investigations showed that it had no significant impact on the angular emission profile and the hemisphere could be used for production. Furthermore, in the glass hemispheres of 09 and 16 cracks were discovered. The affected glass hemispheres were dismounted from the corresponding POCAM devices and were replaced by others.

14 hemispheres were accepted and fully characterized. The first produced POCAM produced, 01, containing hemispheres 01 and 02 was brought to Michigan for further device tests at the Northern Test Site (NTS). The remaining six fully characterized and assembled devices, that are listed in table 5.3, make up the first batch of POCAMs that will be used for the IceCube Upgrade. Currently there is no POCAM device 07, as the pressure housing number 07 was removed and was not used for production.

The characterization of all completed POCAMs included the determination of the isotropy of the angular emission profile for every hemisphere, the total number of emitted photons, as well as the spectral distribution and time profile for every emitter, using different parameter settings. Table 5.3 shows to which percentage each of the six POCAM devices, that belong to the first batch, can emit isotropic light. Tables 5.4 and 5.5 give a selection of values on the number of emitted photons that are achievable with POCAM. Similary, tables 5.6 and 5.7 show how examples for the behavior of the spectral distributions. Lastly, the tables 5.8 and 5.9 give examples for the pulse widths of the time profiles that are typically achievable.

	POCAM 02	POCAM 03	POCAM 04	POCAM 05	POCAM 06	POCAM 08
Hemispheres	09 & 10	11 & 12	13 & 16	18 & 20	19 & 22	23 & 24
Isotropy	5.3 %	6.1 %	7.0 %	6.1 %	6.7 %	7.9 %

Table 5.3.: Isotropy of the angular emission profiles of the six POCAM devices for the first batch. The values give the maximum deviation from perfect isotropic emission, normalized to the averaged angular emission intensity of the devices, respectively.

Hemisphere 23		
	Temperature [°C]	**Number of Photons**
LMG365	25	2.1×10^8
	-20	1.4×10^8
LMG405	25	2.2×10^{10}
	-20	1.9×10^{10}
LMG450	25	2.1×10^{10}
	-20	1.5×10^{10}
LMG520	25	6.4×10^9
	-20	6.3×10^9
KAPU405	25	7.0×10^8
	-20	4.2×10^8
KAPU465	25	9.3×10^8
	-20	8.5×10^8

Table 5.4.: Number of emitted photons per pulse at two different temperatures using the same emitter settings. The values are calculated for the emission intensities of the hemisphere while being operated at PWM= 54000, coarse= 2 and fine= 20 or default mode, respectively.

Hemisphere 24		
	Temperature [°C]	**Number of Photons**
LMG365	25	2.1×10^8
	-20	1.3×10^8
LMG405	25	2.3×10^{10}
	-20	2.0×10^{10}
LMG450	25	2.2×10^{10}
	-20	1.6×10^{10}
LMG520	25	6.1×10^9
	-20	5.9×10^9
KAPU405	25	6.3×10^8
	-20	3.1×10^8
KAPU465	25	9.3×10^8
	-20	8.8×10^8

Table 5.5.: Number of emitted photons per pulse at two different temperatures using the same emitter settings. The values are calculated for the emission intensities of the hemisphere while being operated at PWM= 54000, coarse= 2 and fine= 20 or default mode, respectively.

Hemisphere 23		
	Temperature [°C]	**CWL − FWHM [nm]**
LMG365	25	369.7 − 19.5
	-20	368.5 − 17.5
LMG405	25	404.8 − 9.5
	-20	402.3 − 9.5
LMG450	25	443.3 − 9.5
	-20	441.4 − 9.7
LMG520	25	518.5 − 10.3
	-20	517.9 − 10.1
KAPU405	25	402.2 − 17.1
	-20	401.2 − 15.5
KAPU465	25	459.3 − 29.7
	-20	456.5 − 31.2

Table 5.6.: CWL and FWHM parameters from fitting the spectral distribution at two different temperatures. The values are calculated for the light emission of the hemisphere while being operated at PWM= 54000, coarse= 2 and fine= 20 or default mode, respectively.

Hemisphere 24		
	Temperature [°C]	**CWL − FWHM [nm]**
LMG365	25	369.6 − 19.5
	-20	368.5 − 17.4
LMG405	25	405.9 − 9.5
	-20	403.4 − 9.4
LMG450	25	443.7 − 9.5
	-20	441.7 − 9.7
LMG520	25	514.9 − 10.1
	-20	514.3 − 10.1
KAPU405	25	402.6 − 16.8
	-20	401.7 − 16.2
KAPU465	25	461.1 − 28.0
	-20	458.4 − 29.5

Table 5.7.: CWL and FWHM parameters from fitting the spectral distribution at two different temperatures. The values are calculated for the light emission of the hemisphere while being operated at PWM= 54000, coarse= 2 and fine= 20 or default mode, respectively.

Hemisphere 23		
	Pulse Shape Setting	**FWHM [ns]**
LMG365	2-20	7.1
	1-20	4.9
	1-5	3.4
	0-47	/
LMG405	2-20	9.5
	1-20	6.7
	1-5	5.0
	0-47	2.8
LMG450	2-20	9.8
	1-20	6.6
	1-5	4.7
	0-47	14.6
LMG520	2-20	16.0
	1-20	12.2
	1-5	12.9
	0-47	/
KAPU405	default	7.9
	fast	3.5
KAPU465	default	9.6
	fast	4.0

Table 5.8.: FWHM from fitting the time profiles for the tested pulse shape settings. The values are calculated for the light emission of the hemisphere while being operated at -20 °C and PWM= 54000. A / indicates that no FWHM parameter could be deduced.

Hemisphere 24		
	Pulse Shape Setting	**FWHM [ns]**
LMG365	2-20	7.6
	1-20	4.8
	1-5	3.4
	0-47	/
LMG405	2-20	9.6
	1-20	6.7
	1-5	4.9
	0-47	2.3
LMG450	2-20	9.7
	1-20	6.5
	1-5	4.4
	0-47	9.5
LMG520	2-20	16.1
	1-20	12.8
	1-5	16.4
	0-47	/
KAPU405	default	8.0
	fast	3.6
KAPU465	default	9.6
	fast	4.0

Table 5.9.: FWHM from fitting the time profiles for the tested pulse shape settings. The values are calculated for the light emission of the hemisphere while being operated at -20 °C and PWM= 54000. A / indicates that no FWHM parameter could be deduced.

The angular calibration and automated temperature-dependent characterization for one hemisphere took 3 hours and 40 hours, respectively. Therefore one complete POCAM device could be fully characterized within 4 - 5 days. For future characterizations in the next batch of POCAMs, the setup will include an external reference light which will enable cross-check the calibration of a POCAM as external properties change; for example, temperature and relative humidity. Furthermore, plans exist to take more data for the characterization of the emission intensity, especially at low light levels to improve the cross-calibration of PMT and PD data. This is important because, Future improvements will also include adding a procedure to calibrate the self-monitoring of the PD and SiPM that are integrated into the devices. However, this is not yet completed as the firmware is being finalized. Additionally, an orientation stage has been produced, which will allow the calibration of the accelerometers and magnetometers that monitor the orientation of the devices. This will be important when determining the orientation of the POCAMs when they are frozen in the ice.

Finally, current investigation include speeding up the calibration procedure by improving the efficiency of the procedure and analysis code.

6. Conclusion

The low-energy extension and re-calibration of the detector that will be provided by the IceCube Upgrade, will improve its physical observations and extend its scientific capabilities. The decreased energy threshold and improved detector sensitivity are expected to make IceCube a competitive experiment in the field of neutrino oscillations. Since the statistical uncertainties in IceCube decrease with progressive operation time, the systematic uncertainties become more and more dominant. The Precision Optical Calibration Module will be deployed as part of the IceCube Upgrade to optically calibrate the detector and determine systematic effects with high precision. The POCAM is a thoroughly calibrated, self-monitoring and isotropic light source that can emit nanosecond light pulses at different intensities and wavelengths.

This thesis presented the characterization procedure including results and important features for the first six production devices. It further gave an overview on the physics background and motivation for the POCAM's development as well as the design and components. The characterization of the devices showed that typically the maximum number of emitted photons per pulse was $\sim 3 \cdot 10^8$ - $3 \cdot 10^{11}$. The characterization also showed that the isotropy was between 5 and 8 %. These intensity and isotropy were dependent on the emitter settings and environmental properties. For the four LD-type driven emitters, the pulse-widths could be set to a multitude of values, reaching down to $\sim$ 2 ns. Throughout the characterization, four distinct settings were used which typically resulted in pulse-widths ranging from 2 - 15 ns. For the remaining two Kapustinky-driven emitters, two distinct pulse-width settings were available, that typically produced 3 - 8 ns pulses. The light was emitted by six L(E)Ds at five different nominal wavelengths of 365, 405, 450, 465 and 520 nm. The true emission spectra were typically centered within $\pm$10 nm of the nominal wavelength, and were in agreement with the manufacturers' production uncertainty.

The raw and processed data, taken throughout the characterization procedures, will be provided in a database that is accessible for the IceCube Collaboration. The database is currently under construction and will contain the most important information gathered from the processed characterization data for each of the emitters. This includes the number of emitted photons per pulse, the emission wavelength and the time width of the emitted pulses. For more detailed information on the performance of the emitters, the exact profiles and raw data may be accessed as well.

25 POCAM devices are planned to be characterized and shipped to the South Pole, of which 21 will be deployed on the Upgrade strings in the 2025/26 austral summer season. The first six characterized devices, which were the basis of this work, were shipped from TUM on August 1st 2024 and are expected to arrive at the South Pole in the work season of 2024/25. The final production and characterization of the remaining POCAM devices will start late 2024 and is aimed to be completed by summer 2025, such that all devices are shipped and ready for deployment.

Before the deployment, it is planned to conduct simulation studies based on the characterized POCAM properties and uncertainties, to predict the associated improvements on oscillation parameters for future IceCube analyses. Earlier simulation efforts showed that by using POCAMs, calibration precisions of 1 - 3 % for the given detector systematics, including ice properties and DOM efficiencies, are achievable. This resulted in a predicted improvement of 8 - 30 % on oscillation parameters, compared to previous analyses [10].

A. Appendix

A.1. Relative Humidity inside the Freezer

During first test runs of temperature cycles in the freezer, external temperature and humidity sensors were placed inside to cross-check the ambient temperature with the one that is set by the freezer and to verify that by flushing gaseous nitrogen, the humidity can be removed down to sufficient values. The measured temperature values have been in good agreement with the ones that were set. Nevertheless, throughout the characterization, the temperature sensors of POCAM are read out to monitor the temperature on the boards. The behaviour of the humidity has been explicitly followed for a temperature cycle to the typical temperatures that are set throughout the characterization. The following figures shows the relative humidity during the cool down and warm up phases of the freezer while flushing nitrogen.

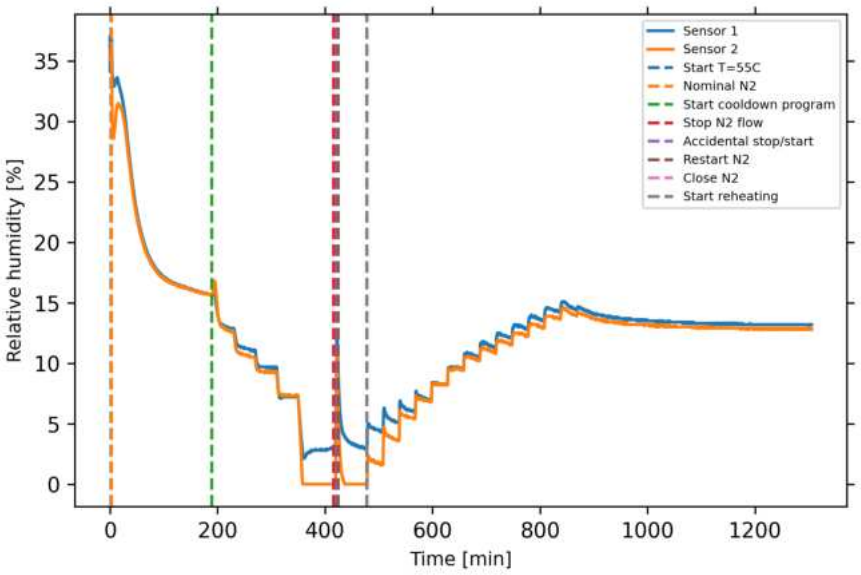

Figure A.1.: Relative humidity inside the freezer for a cooling down to the typical temperature values and warming up again afterwards. During the process nitrogen is flushed into the freezer.

A.2. Skew Normal Distribution

The skew normal distribution, that is used to fit the spectral and time profiles of the emitted light pulses of POCAM, is used to account for potential tilts and tails that may not be reconstructed by only using a simple Gaussian distribution. The skew normal is mathematically described by

$$f(x, \alpha, \mu, \sigma) \;=\; A\,\frac{1}{\sqrt{2\pi}\sigma}\,\exp\left(-\frac{(x-\mu)^2}{2\sigma^2}\right)\cdot\left[1+\operatorname{erf}\left(\frac{\alpha(x-\mu)}{\sqrt{2}}\right)\right] \tag{A.1}$$

where A is a scaling parameter, α is the characteristic skewing parameter and $\operatorname{erf}(z) = \frac{2}{\sqrt{\pi}}\int_0^z dt\; e^{-t^2}$ is the error function. In the case when the skewing parameter is zero, the function describes the regular normal distribution, where μ and σ give its mean and standard deviation, respectively.

A.3. Poissonian Statistics for Time Profile Reconstructions

The detection of single photons to reconstruct the respective time profiles of the emitted pulses, effectivley reduces to a counting experiment, that can be described by a poisson distribution. The occupancy is basically then the mean number of photons that hit the APD. For a certain occupancy λ, this means that the probability for k photons of the same emitted pulse arriving at the APD is given by

$$P(k) = \frac{\lambda^k}{k!}\,e^{-\lambda} \tag{A.2}$$

The probability that only one single photon arrives at the APD, under the condition that at least one arrives and the pulse is detected, is expressed by

$$\frac{P(k=1)}{P(k\geq 1)} = \frac{P(k=1)}{1-P(k=0)} \tag{A.3}$$

Thus, for assuming an occupancy of 0.1, for 95.08 % of the detected pulses only one single photon arrives at the APD.

A.4. Uncertainty Calculation for Time Profile Reconstructions

The calculation of the uncertainty on the reconstruction of the pulse width is based on the propagation of statistical errors. The main uncertainty comes from the used TDC7200, for which an error of approximately

$$\sigma_1 = 0.200 \text{ ns} \tag{A.4}$$

is given by the manufacturer [46]. Furthermore, the reconstruction is based on a finite number of 9000 single timestamps. For pulse widths that are typically of the order ≤ 20 ns, the error for a Gaussian-shaped distribution can be estimated to

$$\sigma_2 = \frac{20 \text{ ns}}{\sqrt{2 \cdot 9000}} = 0.15 \text{ ns} \tag{A.5}$$

The two effects sum up to a total statistical uncertainty of

$$\sigma_{tot} = \sqrt{\sigma_1^2 + \sigma_2^2} = 0.25 \text{ ns} \tag{A.6}$$

A.5. Total Number of Emitted Photons

The following tables give some examples on the number of emitted photons for the hemispheres of the remaining five POCAM devices, that are part of the first batch. The tables only compare the values of the baseline measurement at 25 °C, PWM= 54000 and coarse= 2, fine= 20 or default mode, respectively, to the values taken at −20 °C for the same emitter settings. To have a full insight on the behavior of the emission intensity and other properties, the database or local storage of the characterization data should be accessed.

Hemisphere 09		
	Temperature [°C]	**Number of Photons***
LMG365	25	2.0×10^8
	-20	1.3×10^8
LMG405	25	1.7×10^{10}
	-20	1.5×10^{10}
LMG450	25	8.8×10^9
	-20	6.4×10^9
LMG520	25	5.1×10^9
	-20	5.3×10^9
KAPU405	25	6.8×10^8
	-20	4.3×10^8
KAPU465	25	8.1×10^8
	-20	7.7×10^8

Table A.1.: Selection of values for the total number of emitted photons.

Hemisphere 10		
	Temperature [°C]	**Number of Photons***
LMG365	25	2.1×10^8
	-20	1.4×10^8
LMG405	25	2.0×10^{10}
	-20	1.8×10^{10}
LMG450	25	2.2×10^{10}
	-20	1.6×10^{10}
LMG520	25	6.2×10^9
	-20	6.3×10^9
KAPU405	25	5.5×10^8
	-20	2.8×10^8
KAPU465	25	8.8×10^8
	-20	8.3×10^8

Table A.2.: Selection of values for the total number of emitted photons.

* The calculation of the number of photons for the hemispheres before number 11 could not be done directly, as the angular calibration and temperature-dependent characterization had no setting that was equal at that time, so the relative emission intensity had to be calculated by using an average conversion factor to get the total number of emitted photons.

Hemisphere 11		
	Temperature [°C]	**Number of Photons**
LMG365	25	2.2×10^8
	-20	1.4×10^8
LMG405	25	1.2×10^{10}
	-20	1.1×10^{10}
LMG450	25	1.9×10^{10}
	-20	1.4×10^{10}
LMG520	25	3.2×10^9
	-20	3.6×10^9
KAPU405	25	7.0×10^8
	-20	4.3×10^8
KAPU465	25	8.8×10^8
	-20	8.3×10^8

Table A.3.: Selection of values for the total number of emitted photons.

Hemisphere 12		
	Temperature [°C]	**Number of Photons**
LMG365	25	1.8×10^8
	-20	1.1×10^8
LMG405	25	1.9×10^{10}
	-20	1.6×10^{10}
LMG450	25	2.0×10^{10}
	-20	1.4×10^{10}
LMG520	25	5.4×10^9
	-20	5.2×10^9
KAPU405	25	5.8×10^8
	-20	3.4×10^8
KAPU465	25	7.6×10^8
	-20	7.2×10^8

Table A.4.: Selection of values for the total number of emitted photons.

Hemisphere 13		
	Temperature [°C]	**Number of Photons**
LMG365	25	3.2×10^8
	-20	3.0×10^8
LMG405	25	2.1×10^{10}
	-20	1.8×10^{10}
LMG450	25	2.1×10^{10}
	-20	1.5×10^{10}
LMG520	25	6.1×10^9
	-20	5.9×10^9
KAPU405	25	6.4×10^8
	-20	3.4×10^8
KAPU465	25	8.3×10^8
	-20	7.9×10^8

Table A.5.: Selection of values for the total number of emitted photons.

Hemisphere 16		
	Temperature [°C]	**Number of Photons**
LMG365	25	2.2×10^8
	-20	1.4×10^8
LMG405	25	2.2×10^{10}
	-20	1.9×10^{10}
LMG450	25	2.2×10^{10}
	-20	1.8×10^{10}
LMG520	25	5.3×10^9
	-20	5.2×10^9
KAPU405	25	6.9×10^8
	-20	4.2×10^8
KAPU465	25	8.9×10^8
	-20	8.6×10^8

Table A.6.: Selection of values for the total number of emitted photons.

Hemisphere 18		
	Temperature [°C]	**Number of Photons**
LMG365	25	2.6×10^8
	-20	1.7×10^8
LMG405	25	2.1×10^{10}
	-20	1.8×10^{10}
LMG450	25	2.0×10^{10}
	-20	1.4×10^{10}
LMG520	25	6.0×10^9
	-20	5.8×10^9
KAPU405	25	6.8×10^8
	-20	3.7×10^8
KAPU465	25	8.8×10^8
	-20	8.3×10^8

Table A.7.: Selection of values for the total number of emitted photons.

Hemisphere 20		
	Temperature [°C]	**Number of Photons**
LMG365	25	2.5×10^8
	-20	1.6×10^8
LMG405	25	2.0×10^{10}
	-20	1.7×10^{10}
LMG450	25	2.0×10^{10}
	-20	1.5×10^{10}
LMG520	25	3.6×10^9
	-20	4.9×10^9
KAPU405	25	7.3×10^8
	-20	4.7×10^8
KAPU465	25	9.2×10^8
	-20	8.6×10^8

Table A.8.: Selection of values for the total number of emitted photons.

Hemisphere 19		
	Temperature [°C]	**Number of Photons**
LMG365	25	2.1×10^8
	-20	1.3×10^8
LMG405	25	2.2×10^{10}
	-20	1.9×10^{10}
LMG450	25	2.1×10^{10}
	-20	1.5×10^{10}
LMG520	25	4.8×10^9
	-20	4.6×10^9
KAPU405	25	5.6×10^8
	-20	2.8×10^8
KAPU465	25	9.2×10^8
	-20	8.7×10^8

Table A.9.: Selection of values for the total number of emitted photons.

Hemisphere 22		
	Temperature [°C]	**Number of Photons**
LMG365	25	1.9×10^8
	-20	1.1×10^8
LMG405	25	1.7×10^{10}
	-20	1.4×10^{10}
LMG450	25	1.8×10^{10}
	-20	1.3×10^{10}
LMG520	25	4.8×10^9
	-20	4.7×10^9
KAPU405	25	5.6×10^8
	-20	3.5×10^8
KAPU465	25	7.0×10^8
	-20	6.4×10^8

Table A.10.: Selection of values for the total number of emitted photons.

A.6. Spectral Distributions

The following tables give some examples on emission spectra for the hemispheres of the remaining five POCAM devices, that are part of the first batch. The tables only compare the values of the baseline measurement at 25 °C, PWM= 54000, pulsePer= 3 and coarse= 2, fine= 20 or default mode, respectively, to the values taken at −20 °C for the same emitter settings. To have a full insight on the behavior of the spectral profiles and other properties, the database or local storage of the characterization data should be accessed.

Hemisphere 09		
	Temperature [°C]	**CWL − FWHM [nm]**
LMG365	25	369.6 − 19.5
	-20	368.4 − 18.0
LMG405	25	405.9 − 9.5
	-20	403.4 − 9.4
LMG450	25	441.9 − 9.9
	-20	440.0 − 9.8
LMG520	25	516.1 − 10.7
	-20	515.6 − 9.9
KAPU405	25	401.9 − 17.1
	-20	400.9 − 15.7
KAPU465	25	461.8 − 27.7
	-20	459.2 − 28.6

Table A.11.: Selection of values for parameters of the emission spectra.

Hemisphere 10		
	Temperature [°C]	**CWL − FWHM [nm]**
LMG365	25	369.7 − 19.5
	-20	368.3 − 16.9
LMG405	25	405.8 − 9.5
	-20	403.3 − 9.4
LMG450	25	441.3 − 9.5
	-20	439.4 − 9.8
LMG520	25	514.3 − 10.2
	-20	513.9 − 10.2
KAPU405	25	403.7 − 17.0
	-20	403.0 − 16.1
KAPU465	25	460.7 − 28.4
	-20	458.1 − 29.6

Table A.12.: Selection of values for parameters of the emission spectra.

Hemisphere 11		
	Temperature [°C]	**CWL − FWHM [nm]**
LMG365	25	369.5 − 19.4
	-20	368.4 − 17.5
LMG405	25	405.3 − 9.5
	-20	402.9 − 9.5
LMG450	25	440.9 − 9.4
	-20	439.0 − 9.6
LMG520	25	517.3 − 10.1
	-20	517.1 − 10.4
KAPU405	25	401.8 − 17.1
	-20	400.7 − 15.6
KAPU465	25	460.8 − 28.3
	-20	458.3 − 29.4

Table A.13.: Selection of values for parameters of the emission spectra.

Hemisphere 12		
	Temperature [°C]	**CWL − FWHM [nm]**
LMG365	25	370.0 − 19.5
	-20	368.7 − 17.1
LMG405	25	405.5 − 9.4
	-20	402.9 − 9.4
LMG450	25	443.1 − 9.5
	-20	441.2 − 9.6
LMG520	25	515.8 − 10.0
	-20	515.2 − 10.0
KAPU405	25	403.2 − 16.9
	-20	402.3 − 15.5
KAPU465	25	460.4 − 28.5
	-20	457.5 − 30.1

Table A.14.: Selection of values for parameters of the emission spectra.

Hemisphere 13		
	Temperature [°C]	**CWL − FWHM [nm]**
LMG365	25	377.5 − 16.3
	-20	375.6 − 16.2
LMG405	25	406.3 − 9.5
	-20	403.8 − 9.5
LMG450	25	442.9 − 9.5
	-20	440.9 − 9.7
LMG520	25	515.0 − 10.0
	-20	514.3 − 10.1
KAPU405	25	402.7 − 16.9
	-20	401.8 − 16.4
KAPU465	25	460.3 − 28.3
	-20	457.2 − 29.7

Table A.15.: Selection of values for parameters of the emission spectra.

Hemisphere 16		
	Temperature [°C]	**CWL − FWHM [nm]**
LMG365	25	370.0 − 19.2
	-20	368.6 − 17.2
LMG405	25	402.7 − 9.5
	-20	400.1 − 9.5
LMG450	25	443.4 − 9.5
	-20	441.5 − 9.4
LMG520	25	515.0 − 10.0
	-20	513.9 − 10.1
KAPU405	25	402.3 − 17.1
	-20	401.2 − 15.7
KAPU465	25	459.3 − 28.3
	-20	456.3 − 29.8

Table A.16.: Selection of values for parameters of the emission spectra.

Hemisphere 18		
	Temperature [°C]	**CWL − FWHM [nm]**
LMG365	25	369.4 − 19.1
	-20	368.2 − 16.7
LMG405	25	405.3 − 9.5
	-20	402.8 − 9.4
LMG450	25	443.6 − 9.5
	-20	441.6 − 9.7
LMG520	25	513.9 − 10.2
	-20	513.3 − 9.9
KAPU405	25	401.6 − 17.2
	-20	400.6 − 15.6
KAPU465	25	460.6 − 28.6
	-20	457.8 − 29.8

Table A.17.: Selection of values for parameters of the emission spectra.

Hemisphere 20		
	Temperature [°C]	**CWL − FWHM [nm]**
LMG365	25	369.4 − 19.3
	-20	368.3 − 17.6
LMG405	25	402.9 − 9.4
	-20	400.5 − 9.5
LMG450	25	443.7 − 9.5
	-20	442.2 − 9.7
LMG520	25	516.9 − 10.2
	-20	517.0 − 10.6
KAPU405	25	401.3 − 17.2
	-20	400.4 − 15.5
KAPU465	25	459.4 − 29.0
	-20	456.7 − 30.3

Table A.18.: Selection of values for parameters of the emission spectra.

Hemisphere 19		
	Temperature [°C]	**CWL − FWHM [nm]**
LMG365	25	369.7 − 19.1
	-20	368.5 − 17.0
LMG405	25	406.1 − 9.5
	-20	403.6 − 9.5
LMG450	25	444.9 − 9.5
	-20	443.2 − 9.7
LMG520	25	517.1 − 10.5
	-20	516.3 − 10.6
KAPU405	25	403.7 − 16.9
	-20	403.1 − 16.1
KAPU465	25	461.4 − 28.3
	-20	458.9 − 29.4

Table A.19.: Selection of values for parameters of the emission spectra.

Hemisphere 22		
	Temperature [°C]	**CWL − FWHM [nm]**
LMG365	25	370.7 − 18.7
	-20	369.4 − 16.3
LMG405	25	406.0 − 9.4
	-20	403.6 − 9.4
LMG450	25	443.8 − 9.4
	-20	442.0 − 9.5
LMG520	25	517.6 − 10.5
	-20	517.1 − 10.6
KAPU405	25	402.4 − 16.7
	-20	401.4 − 15.6
KAPU465	25	458.6 − 29.3
	-20	455.1 − 31.2

Table A.20.: Selection of values for parameters of the emission spectra.

A.7. Time Profiles

The following tables give some examples on the pulse widths for the time profiles for the hemispheres of the remaining five POCAM devices, that are part of the first batch. The tables only compare the FWHM for the tested pulse-width settings that are taken at -20 °C and PWM= 54000 and pulsePer= 3 (or 30). If the time profile could not be taken, a "/" is inserted. Especially for earlier tested hemispheres, like 09 and 10, the time profile could not be taken for emitters and parameter settings that showed very faint light intensities. For later tested hemispheres, the light yield was increased by the glass rod, such that more time profiles could be reconstructed. To have a full insight on the behavior of the spectral profiles and other properties, the database or local storage of the characterization data should be accessed.

Hemisphere 09		
	Pulse Shape Setting	**FWHM [ns]**
LMG365	2-20	7.6
	1-20	/
	1-5	/
	0-47	/
LMG405	2-20	9.7
	1-20	/
	1-5	/
	0-47	37.5
LMG450	2-20	7.4
	1-20	/
	1-5	3.6
	0-47	/
LMG520	2-20	17.3
	1-20	/
	1-5	19.2
	0-47	/
KAPU405	default	7.8
	fast	3.5
KAPU465	default	9.5
	fast	4.1

Table A.21.: Selection of values for determined pulse widths.

Hemisphere 10		
	Pulse Shape Setting	**FWHM [ns]**
LMG365	2-20	7.7
	1-20	/
	1-5	3.3
	0-47	/
LMG405	2-20	9.6
	1-20	/
	1-5	/
	0-47	15.8
LMG450	2-20	9.4
	1-20	/
	1-5	4.3
	0-47	15.9
LMG520	2-20	16.0
	1-20	/
	1-5	/
	0-47	/
KAPU405	default	8.2
	fast	/
KAPU465	default	9.4
	fast	4.1

Table A.22.: Selection of values for determined pulse widths.

Hemisphere 11		
	Pulse Shape Setting	**FWHM [ns]**
LMG365	2-20	7.7
	1-20	4.6
	1-5	3.2
	0-47	/
LMG405	2-20	8.0
	1-20	5.8
	1-5	/
	0-47	/
LMG450	2-20	9.5
	1-20	6.2
	1-5	4.3
	0-47	18.0
LMG520	2-20	15.1
	1-20	33.4
	1-5	34.2
	0-47	/
KAPU405	default	/
	fast	3.4
KAPU465	default	9.6
	fast	4.0

Table A.23.: Selection of values for determined pulse widths.

Hemisphere 12		
	Pulse Shape Setting	**FWHM [ns]**
LMG365	2-20	7.7
	1-20	4.8
	1-5	3.3
	0-47	/
LMG405	2-20	9.4
	1-20	6.6
	1-5	5.0
	0-47	15.7
LMG450	2-20	9.4
	1-20	6.5
	1-5	4.5
	0-47	14.6
LMG520	2-20	16.0
	1-20	13.5
	1-5	16.4
	0-47	27.1
KAPU405	default	7.9
	fast	3.4
KAPU465	default	9.5
	fast	3.9

Table A.24.: Selection of values for determined pulse widths.

Hemisphere 13		
	Pulse Shape Setting	**FWHM [ns]**
LMG365	2-20	7.2
	1-20	4.6
	1-5	3.5
	0-47	/
LMG405	2-20	9.6
	1-20	6.5
	1-5	/
	0-47	15.2
LMG450	2-20	9.5
	1-20	6.4
	1-5	4.4
	0-47	13.1
LMG520	2-20	16.5
	1-20	12.2
	1-5	15.8
	0-47	/
KAPU405	default	7.9
	fast	3.5
KAPU465	default	/
	fast	4.0

Table A.25.: Selection of values for determined pulse widths.

Hemisphere 16		
	Pulse Shape Setting	**FWHM [ns]**
LMG365	2-20	7.8
	1-20	5.0
	1-5	3.4
	0-47	/
LMG405	2-20	9.6
	1-20	6.7
	1-5	5.3
	0-47	3.0
LMG450	2-20	9.1
	1-20	6.4
	1-5	4.7
	0-47	/
LMG520	2-20	16.1
	1-20	12.4
	1-5	11.9
	0-47	25.0
KAPU405	default	7.9
	fast	3.5
KAPU465	default	9.3
	fast	3.9

Table A.26.: Selection of values for determined pulse widths.

Hemisphere 18		
	Pulse Shape Setting	**FWHM [ns]**
LMG365	2-20	7.7
	1-20	4.5
	1-5	3.1
	0-47	/
LMG405	2-20	9.6
	1-20	6.4
	1-5	5.2
	0-47	/
LMG450	2-20	9.4
	1-20	6.1
	1-5	4.3
	0-47	/
LMG520	2-20	16.1
	1-20	12.9
	1-5	15.3
	0-47	/
KAPU405	default	8.1
	fast	3.5
KAPU465	default	9.7
	fast	4.0

Table A.27.: Selection of values for determined pulse widths.

Hemisphere 20		
	Pulse Shape Setting	**FWHM [ns]**
LMG365	2-20	7.5
	1-20	4.7
	1-5	3.3
	0-47	/
LMG405	2-20	9.4
	1-20	6.3
	1-5	4.9
	0-47	/
LMG450	2-20	9.4
	1-20	6.3
	1-5	4.3
	0-47	/
LMG520	2-20	18.4
	1-20	15.4
	1-5	18.4
	0-47	/
KAPU405	default	7.9
	fast	3.5
KAPU465	default	9.7
	fast	3.9

Table A.28.: Selection of values for determined pulse widths.

Hemisphere 19		
	Pulse Shape Setting	**FWHM [ns]**
LMG365	2-20	7.4
	1-20	4.7
	1-5	3.3
	0-47	/
LMG405	2-20	9.4
	1-20	6.7
	1-5	4.8
	0-47	11.2
LMG450	2-20	9.3
	1-20	6.3
	1-5	4.4
	0-47	12.1
LMG520	2-20	16.7
	1-20	14.6
	1-5	17.3
	0-47	/
KAPU405	default	8.0
	fast	3.5
KAPU465	default	9.3
	fast	4.1

Table A.29.: Selection of values for determined pulse widths.

Hemisphere 22		
	Pulse Shape Setting	**FWHM [ns]**
LMG365	2-20	7.4
	1-20	4.6
	1-5	3.2
	0-47	/
LMG405	2-20	9.3
	1-20	6.5
	1-5	5.0
	0-47	/
LMG450	2-20	9.4
	1-20	6.2
	1-5	4.2
	0-47	/
LMG520	2-20	17.7
	1-20	14.9
	1-5	19.3
	0-47	/
KAPU405	default	7.7
	fast	3.3
KAPU465	default	9.7
	fast	3.9

Table A.30.: Selection of values for determined pulse widths.

A.8. Emitter Selection

Emitter	Vendor	Wavelength [nm]	Type
XSL-365-5E	Roithner Lasertechnik	365 ± 8	LED
XRL-400-5E	Roithner Lasertechnik	405 ± 8	LED
RLT405500MG	Roithner Lasertechnik	405 ± 5	LD
PL-TB450B	Laser Components	450 ± 10	LD
NSPB300B	Nichia Corporation	465 ± 7	LED
PLT5 520_B1-3	OSRAM	520 ± 10	LD

Figure A.2.: Summary of the emitters that are installed on each hemisphere.

A.9. Glass Hemisphere Cracking after Assembly

Figure A.3 shows one of the two glass hemispheres that cracked after the assembly of the corresponding POCAM device. The hemispheres were dismounted and replaced by others.

Figure A.3.: Cracking glass hemisphere which appeared after assembly and had to be replaced.

A.10. Orientation Calibration Stage

Figure A.4 shows the recently added orientation stage, that is used to calibrate the self-monitoring accelerometer and magnetometer sensors on the POCAM devices.

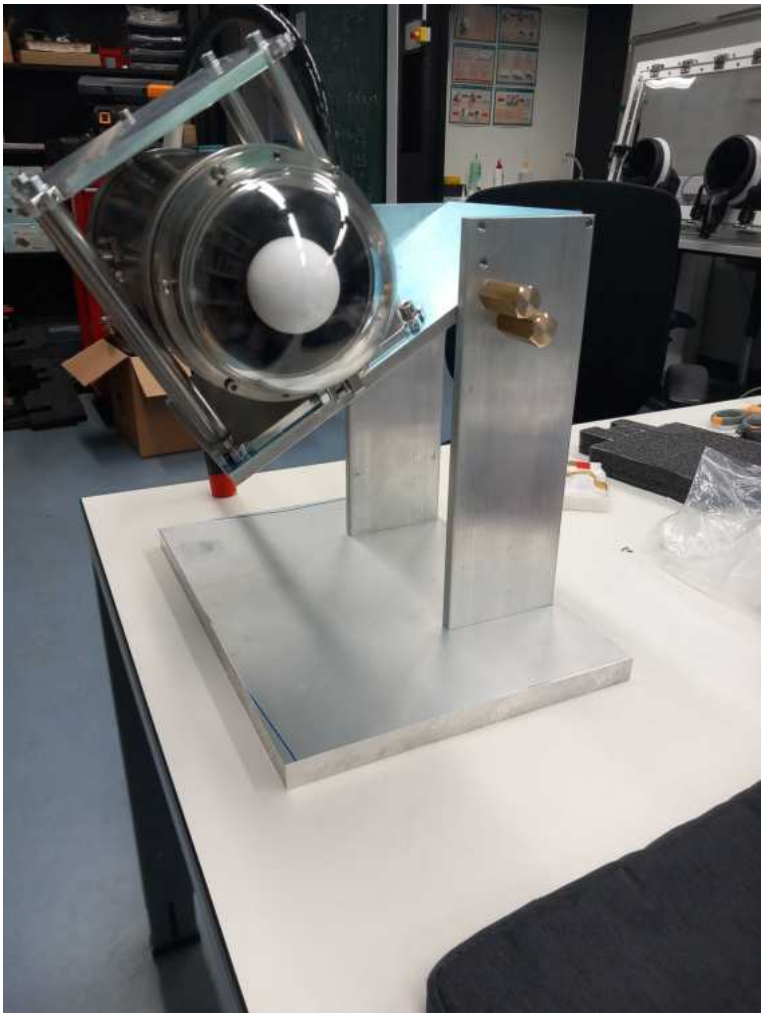

Figure A.4.: Orientation stage to calibrate the accelerometer and magnetometer of the POCAM devices.

List of Figures

List of Tables

Bibliography

[1] M. A. et al. "Neutrino emission from the direction of the blazar TXS 0506056 prior to the IceCube-170922A alert". In: *Science* 361.6398 (July 2018), pp. 147–151. DOI: 10.1126/science.aat2890. URL: https://doi.org/10.1126/science.aat2890.

[2] P. Padovani et al. "PKS1424+240: yet another masquerading BL Lac object as a possible IceCube neutrino source". In: *Monthly Notices of the Royal Astronomical Society* 511.4 (Feb. 2022), pp. 4697–4701. ISSN: 1365-2966. DOI: 10.1093/mnras/stac376. URL: http://dx.doi.org/10.1093/mnras/stac376.

[3] I. Collaboration*† et al. "Evidence for neutrino emission from the nearby active galaxy NGC 1068". In: *Science* 378.6619 (2022), pp. 538–543. DOI: 10.1126/science.abg3395. eprint: https://www.science.org/doi/pdf/10.1126/science.abg3395. URL: https://www.science.org/doi/abs/10.1126/science.abg3395.

[4] K. Anderson et al. "A New Nuclear Reactor Neutrino Experiment to Measure 13". In: *arXiv* (2004). arXiv: physics/0404071 [physics]. URL: https://arxiv.org/pdf/physics/0404071.

[5] D. B. collaboration et al. *Precision measurement of reactor antineutrino oscillation at kilometer-scale baselines by Daya Bay*. 2022. arXiv: 2211.14988 [hep-ex]. URL: https://arxiv.org/abs/2211.14988.

[6] R. Davis. "A review of the homestake solar neutrino experiment". In: *Progress in Particle and Nuclear Physics* 32 (1994), pp. 13–32. ISSN: 0146-6410. DOI: https://doi.org/10.1016/0146-6410(94)90004-3. URL: https://www.sciencedirect.com/science/article/pii/0146641094900043.

[7] A. Bellerive et al. "The Sudbury Neutrino Observatory". In: *Nuclear Physics B* 908 (July 2016), pp. 30–51. ISSN: 0550-3213. DOI: 10.1016/j.nuclphysb.2016.04.035. URL: http://dx.doi.org/10.1016/j.nuclphysb.2016.04.035.

[8] K. Abe et al. "Solar neutrino measurements using the full data period of Super-Kamiokande-IV". In: *Physical Review D* 109.9 (May 2024). ISSN: 2470-0029. DOI: 10.1103/physrevd.109.092001. URL: http://dx.doi.org/10.1103/PhysRevD.109.092001.

[9] T. K. Gaisser, R. Engel, and E. Resconi. *Cosmic Rays and Particle Physics*. 2nd ed. Cambridge University Press, 2016.

[10] F. Henningsen. "The self-monitoring precision calibration light source for the IceCube Upgrade". en. PhD thesis. Technische Universität München, 2021, p. 149. URL: https://mediatum.ub.tum.de/1632649.

[11] K. Greisen. "End to the Cosmic-Ray Spectrum?" In: *Phys. Rev. Lett.* 16 (17 Apr. 1966), pp. 748–750. DOI: 10.1103/PhysRevLett.16.748. URL: https://link.aps.org/doi/10.1103/PhysRevLett.16.748.

[12] G. T. Zatsepin and V. A. Kuzmin. "Upper limit of the spectrum of cosmic rays". In: *JETP Lett.* 4 (1966), pp. 78–80.

[13] P. D. Group. *Review of Particle Physics: Charm Mesons*. Accessed: 2024-07-19. 2016. URL: https://pdg.lbl.gov/2016/tables/rpp2016-tab-mesons-charm.pdf.

[14] T. K. Gaisser. *Atmospheric Neutrinos*. 2019. arXiv: 1910.08851 [astro-ph.HE]. URL: https://arxiv.org/abs/1910.08851.

[15] C. Mascaretti and F. Vissani. "On the relevance of prompt neutrinos for the interpretation of the IceCube signals". In: *Journal of Cosmology and Astroparticle Physics* 2019.08 (Aug. 2019), pp. 004–004. ISSN: 1475-7516. DOI: 10.1088/1475-7516/2019/08/004. URL: http://dx.doi.org/10.1088/1475-7516/2019/08/004.

[16] I. Collaboration*. "Evidence for High-Energy Extraterrestrial Neutrinos at the IceCube Detector". In: *Science* 342.6161 (2013), p. 1242856. DOI: 10.1126/science.1242856. eprint: https://www.science.org/doi/pdf/10.1126/science.1242856. URL: https://www.science.org/doi/abs/10.1126/science.1242856.

[17] M. G. Aartsen et al. "OBSERVATION AND CHARACTERIZATION OF A COSMIC MUON NEUTRINO FLUX FROM THE NORTHERN HEMISPHERE USING SIX YEARS OF ICECUBE DATA". In: *The Astrophysical Journal* 833.1 (Dec. 2016), p. 3. DOI: 10.3847/0004-637X/833/1/3. URL: https://dx.doi.org/10.3847/0004-637X/833/1/3.

[18] M. A. et al. "Multimessenger observations of a flaring blazar coincident with high-energy neutrino IceCube-170922A". In: *Science* 361.6398 (July 2018). DOI: 10.1126/science.aat1378. URL: https://doi.org/10.1126/science.aat1378.

[19] R. Abbasi et al. "Observation of high-energy neutrinos from the Galactic plane". In: *Science* 380.6652 (June 2023), pp. 1338–1343. ISSN: 1095-9203. DOI: 10.1126/science.adc9818. URL: http://dx.doi.org/10.1126/science.adc9818.

[20] University of Wisconsin–Madison. *IceCube shows Milky Way galaxy is a 'neutrino desert'*. Accessed: 2024-08-11. 2024. URL: https://news.wisc.edu/icecube-shows-milky-way-galaxy-is-a-neutrino-desert/.

[21] Heidelberg University Physics Department. *Quantum Field Theory Lecture Notes*. Accessed: 2024-08-01. 2024. URL: https://uebungen.physik.uni-heidelberg.de/vorlesung/20241/1848.

[22] A. J. Larkoski. *Elementary Particle Physics*. Cambridge University Press, May 2019. DOI: 10.1017/9781108633758. URL: https://doi.org/10.1017/9781108633758.

[23] U. Author. *Majorana and Dirac Neutrinos*. Accessed: 2024-08-01. 2024. URL: https://www.if.ufrj.br/~jtmn/journal_club_Astrop/Majorana_and_Dirac_Neutrinos.pdf.

[24] N. Abgrall et al. "The large enriched germanium experiment for neutrinoless double beta decay (LEGEND)". In: *AIP Conference Proceedings*. Author(s), 2017. DOI: 10.1063/1.5007652. URL: http://dx.doi.org/10.1063/1.5007652.

[25] A. F. Daneri. *Dissertation*. Accessed: 2024-08-01. 2023. URL: https://www.imperial.ac.uk/media/imperial-college/research-centres-and-groups/theoretical-physics/msc/dissertations/2023/Albert-Forsyth-Daneri-Dissertation.pdf.

[26] C. Giunti and C. W. Kim. *Fundamentals of Neutrino Physics and Astrophysics*. ProQuest Ebook Central. Oxford University Press, Incorporated, 2007. URL: https://ebookcentral-proquest-com.eaccess.tum.edu/lib/munchentech/detail.action?docID=415331.

[27] A. Terliuk. "Measurement of atmospheric neutrino oscillations and search for sterile neutrino mixing with IceCube DeepCore". PhD thesis. Humboldt-Universität zu Berlin, Mathematisch-Naturwissenschaftliche Fakultät, 2018. DOI: http://dx.doi.org/10.18452/19304.

[28] Z. Maki, M. Nakagawa, and S. Sakata. "Remarks on the Unified Model of Elementary Particles". In: *Progress of Theoretical Physics* 28.5 (Nov. 1962), pp. 870–880. DOI: 10.1143/ptp.28.870. URL: https://doi.org/10.1143/ptp.28.870.

[29] B. Pontecorvo. *Neutrino Experiments and the Problem of Conservation of Leptonic Charge*. 1967.

[30] S. Sharma et al. In: *Journal of Physics: Conference Series* 556.1 (2023), p. 012060. DOI: 10.1088/1742-6596/556/1/012060. URL: https://iopscience.iop.org/article/10.1088/1742-6596/556/1/012060.

[31] S. Davidson, E. Nardi, and Y. Nir. "Leptogenesis". In: *Physics Reports* 466.4–5 (Sept. 2008), pp. 105–177. ISSN: 0370-1573. DOI: 10.1016/j.physrep.2008.06.002. URL: http://dx.doi.org/10.1016/j.physrep.2008.06.002.

[32] G. Fogli and E. Lisi. "Evidence for the MSW effect". In: *New Journal of Physics* 6.1 (Oct. 2004), p. 139. DOI: 10.1088/1367-2630/6/1/139. URL: https://dx.doi.org/10.1088/1367-2630/6/1/139.

[33] A. Y. Smirnov. *The MSW effect and Solar Neutrinos*. 2003. arXiv: hep-ph/0305106 [hep-ph]. URL: https://arxiv.org/abs/hep-ph/0305106.

[34] I. Collaboration. *Measurement of atmospheric neutrino oscillation parameters using convolutional neural networks with 9.3 years of data in IceCube DeepCore*. 2024. arXiv: 2405.02163 [hep-ex]. URL: https://arxiv.org/abs/2405.02163.

[35] P. D. Group et al. "Review of Particle Physics". In: *Progress of Theoretical and Experimental Physics* 2022.8 (Aug. 2022), p. 083C01. ISSN: 2050-3911. DOI: 10.1093/ptep/ptac097. eprint: https://academic.oup.com/ptep/article-pdf/2022/8/083C01/49175550/ptac097_11_hypothetical_particles_and_concepts.pdf. URL: https://doi.org/10.1093/ptep/ptac097.

[36] IceCube Neutrino Observatory. *Research*. Accessed: 2024-08-02. 2024. URL: https://icecube.wisc.edu/science/research/.

[37] M. Aartsen et al. "The IceCube Neutrino Observatory: Instrumentation and Online Systems". In: *Journal of Instrumentation* 12 (2017), P03012. DOI: 10.1088/1748-0221/12/03/P03012. arXiv: 1612.05093 [astro-ph.IM]. URL: https://arxiv.org/abs/1612.05093.

[38] P. D. Group et al. "Review of Particle Physics". In: *Progress of Theoretical and Experimental Physics* 2020.8 (Aug. 2020), p. 083C01. ISSN: 2050-3911. DOI: 10.1093/ptep/ptaa104. eprint: https://academic.oup.com/ptep/article-pdf/2020/8/083C01/34673722/ptaa104.pdf. URL: https://doi.org/10.1093/ptep/ptaa104.

[39] J. A. Formaggio and G. P. Zeller. "From eV to EeV: Neutrino cross sections across energy scales". In: *Reviews of Modern Physics* 84.3 (Sept. 2012), pp. 1307–1341. DOI: 10.1103/revmodphys.84.1307. URL: https://doi.org/10.1103/revmodphys.84.1307.

[40] I. Frank and I. Tamm. *Coherent Visible Radiation of Fast Electrons Passing Through Matter*. Ed. by B. Bolotovskii, V. Frenkel, and R. Peierls. Berlin, Heidelberg: Springer, 1991, pp. 29–34. DOI: 10.1007/978-3-642-74626-0_2. URL: https://doi.org/10.1007/978-3-642-74626-0_2.

[41] T. Anderson et al. *Design and performance of the multi-PMT optical module for IceCube Upgrade*. 2021. arXiv: 2107.11383 [astro-ph.IM]. URL: https://arxiv.org/abs/2107.11383.

[42] R. Abbasi et al. "D-Egg: a dual PMT optical module for IceCube". In: *Journal of Instrumentation* 18.04 (Apr. 2023), P04014. ISSN: 1748-0221. DOI: 10.1088/1748-0221/18/04/p04014. URL: http://dx.doi.org/10.1088/1748-0221/18/04/P04014.

[43] W. Kang, C. Tönnis, and C. Rott. *The camera system for the IceCube Upgrade*. 2019. arXiv: 1908.07734 [astro-ph.IM]. URL: https://arxiv.org/abs/1908.07734.

[44] D. Heinen et al. *An Acoustic Calibration System for the IceCube Upgrade*. 2019. arXiv: 1909.02047 [astro-ph.IM]. URL: https://arxiv.org/abs/1909.02047.

[45] N. Khera and F. Henningsen. *POCAM in the IceCube Upgrade*. 2021. arXiv: 2108.05298 [astro-ph.HE]. URL: https://arxiv.org/abs/2108.05298.

[46] Texas Instruments. *TDC7200: Time-to-Digital Converter for Time-of-Flight Applications*. Accessed: 2024-08-21. Aug. 2017. URL: https://www.ti.com/lit/ds/symlink/tdc7200.pdf.

[47] L. Eidenschink. *Assembly and Characterization of the First Precision Optical Calibration Module for the IceCube-Upgrade*. 2024.

[48] P. B. Price et al. "Temperature profile for glacial ice at the South Pole: Implications for life in a nearby subglacial lake". In: *Proceedings of the National Academy of Sciences* 99.12 (2002), pp. 7844–7847. DOI: 10.1073/pnas.082238999. eprint: https://www.pnas.org/doi/pdf/10.1073/pnas.082238999. URL: https://www.pnas.org/doi/abs/10.1073/pnas.082238999.

Acknowledgements

Initially I want to thank my supervising professor, Elisa Resconi, for giving me the opportunity to work on the POCAM project. After finishing my Bachelor's degree under your supervision, it was the second time that I had the joy to be part of your group and work in the field of neutrino astronomy, Grazie mille.

Special gratitude goes out to Andrii Terliuk for supervising the project. Thank You for all your effort on advising me throughout the last year. I highly appreciate You not only as the great scientist You are, but also as an inspiring person.

Many thanks as well to Philipp Eller for your work on the project and especially your help on completing my thesis but also for the nice person You are.

Thank You Sim Bash for your contributions to the project throughout the last year and for bringing the comedy to Germany. I want to thank You in particular for your help and advices during the writing process for my thesis. I am looking forward to see You again when You will return from the South Pole, Servus Bra.
P.S.: Thanks for making me look like the greatest pool player of all time.

A big thank You goes to my office mate Leonhard Eidenschink with whom I worked together on this project the most. Thanks for all the productive and also funny discussions we had.

The last words I want to dedicate to my family. I thought long about what to tell You that would express my feelings and thoughts I have, but these short words could never describe what happened in the last 27 years, what goes far beyond my studies in physics. So I will just say Thank You for all the good things I have experienced so far and for staying by my side.